MNRAS 000, 1–22 (2019) Preprint 25 September 2019 Compiled using MNRAS LATEX style file v3.0

Calibration of the mixing length theory for structures of helium-dominated atmosphere white dwarfs

E. Cukanovaite[1] ★, P.-E. Tremblay[1], B. Freytag[2], H.-G. Ludwig[3], G. Fontaine[4], P. Brassard[4], O. Toloza[1] and D. Koester[5]

[1] *Department of Physics, University of Warwick, Coventry CV4 7AL, UK*
[2] *Department of Physics and Astronomy, Uppsala University, Box 516, 751 20 Uppsala, Sweden*
[3] *Zentrum für Astronomie der Universität Heidelberg, Landessternwarte, Königstuhl 12, 69117 Heidelberg, Germany*
[4] *Département de Physique, Université de Montréal, C.P. 6128, Succ. Centre-Ville, Montréal, QC H3C 3J7, Canada*
[5] *Institut für Theoretische Physik und Astrophysik, Universität Kiel, 24098 Kiel, Germany*

Accepted XXX. Received YYY; in original form ZZZ

ABSTRACT

We perform a calibration of the mixing length parameter at the bottom boundary of the convection zone for helium-dominated atmospheres of white dwarfs. This calibration is based on a grid of 3D DB (pure-helium) and DBA (helium-dominated with traces of hydrogen) model atmospheres computed with the CO^{5}BOLD radiation-hydrodynamics code, and a grid of 1D DB and DBA envelope structures. The 3D models span a parameter space of hydrogen-to-helium abundances between $-10.0 \leqslant \log(\mathrm{H/He}) \leqslant -2.0$, surface gravities between $7.5 \leqslant \log g \leqslant 9.0$ and effective temperatures between $12\,000$ K $\lesssim T_{\rm eff} \lesssim 34\,000$ K. The 1D envelopes cover a similar atmospheric parameter range, but are also calculated with different values of the mixing length parameter, namely $0.4 \leqslant \mathrm{ML2}/\alpha \leqslant 1.4$. The calibration is performed based on two definitions of the bottom boundary of the convection zone, the Schwarzschild and the zero convective flux boundaries. Thus, our calibration is relevant for applications involving the bulk properties of the convection zone including its total mass, which excludes the spectroscopic technique. Overall, the calibrated ML2/α is smaller than what is commonly used in evolutionary models and theoretical determinations of the blue edge of the instability strip for pulsating DB and DBA stars. With calibrated ML2/α we are able to deduce more accurate convection zone sizes needed for studies of planetary debris mixing and dredge-up of carbon from the core. We highlight this by calculating examples of metal-rich 3D DBAZ models and finding their convection zone masses. Mixing length calibration represents the first step of in-depth investigations of convective overshoot in white dwarfs with helium-dominated atmospheres.

Key words: asteroseismology – convection – hydrodynamics – stars: atmospheres – white dwarfs

1 INTRODUCTION

Any main-sequence star below $\approx 8M_\odot$ will end its life by expelling the majority of its outer envelope and leaving behind a dense, degenerate core, known as a white dwarf (Althaus et al. 2010). Due to their large surface gravities (abbreviated as the logarithm of surface gravity, $\log g$), compositionally these stellar remnants are well-stratified, with the heavier material sinking into the core and the outer layers being composed of the lightest chemical elements present (Schatzman 1948). In magnitude-limited samples around 80% of all white dwarfs have hydrogen-dominated atmospheres and 20% have helium-dominated atmospheres (Kleinman et al. 2013; Kepler et al. 2015). White dwarfs are unable to fuse matter in their degenerate cores and thus evolve simply by cooling. As they cool, superficial convection zones develop in their envelopes and grow bigger with decreasing effective temperature, $T_{\rm eff}$ (Tassoul et al. 1990). This means that both the structure and evolutionary models of white dwarfs can be affected by uncertainties arising from the treatment of convective energy transport.

Until recently, the standard white dwarf models used for the atmosphere and the interior have been 1D, where convection is treated using the ML2 version (Tassoul et al. 1990) of

★ E-mail: E.Cukanovaite@warwick.ac.uk

the mixing length theory, MLT (Böhm-Vitense 1958). The formulation of this theory assumes same-sized, large convective eddies travelling a distance, d, which is known as the mixing length, before dissipating into the surroundings by releasing (or absorbing) their excess (or deficient) energy. The distance travelled depends on a free parameter called the mixing length parameter, α (or ML2/α to indicate the use of ML2 version of MLT for white dwarfs), such that

$$d = \alpha H_{\rm p} \,, \tag{1}$$

where $H_{\rm p}$ is the pressure scale height. This free parameter is not given by the MLT and instead must be calibrated from observations, which is a significant shortcoming of the theory as the particular value of the parameter can have a significant effect on the modelled structures (see examples for both evolutionary and atmospheric models: Shipman 1979; Winget et al. 1982, 1983; Fontaine et al. 1984; Tassoul et al. 1990; Thejll et al. 1991; Bergeron et al. 1992; Koester et al. 1994; Bergeron et al. 1995; Wesemael et al. 1999; Córsico & Althaus 2016), especially when convection becomes superadiabatic (Tremblay et al. 2015; Sonoi et al. 2019).

As an improvement, another 1D theory of convection, CMT (Canuto & Mazzitelli 1991, 1992) and its refined version CGM (Canuto et al. 1996), have also been used in modelling white dwarf evolution (Althaus & Benvenuto 1996, 1997; Benvenuto & Althaus 1999). Unlike MLT, CMT does not rely on the approximation of single-sized convective eddies and instead considers a full range of eddy sizes. Unfortunately, similarly to MLT, CMT depends on the local conditions of the atmosphere (Ludwig et al. 1999), which is a restrictive approximation as convection is a non-local process. This assumption was subsequently removed in non-local 1D envelope models of white dwarfs (Montgomery & Kupka 2004). Given that convection is inherently a 3D process, the dimensionality issue was first improved by 2D atmospheric models of DA white dwarfs developed by Ludwig et al. (1993), Ludwig et al. (1994) and Freytag et al. (1996).

More recently, the first 3D models for pure-hydrogen atmosphere (DA) (Tremblay et al. 2013a,b,c; Kupka et al. 2018) and pure-helium atmosphere (DB) (Cukanovaite et al. 2018) white dwarfs have been developed. In 3D models convection is non-local, is treated from first principles and the models do not depend on any free parameters, although numerical parameters do exist. Spectroscopic corrections derived from 3D models have been tested against *Gaia* DR2 data (Gaia Collaboration et al. 2018) by comparing the observed parallaxes for samples of DA and DB/DBA white dwarfs with spectroscopically-derived parallaxes with and without 3D corrections (Tremblay et al. 2019). 3D DA corrections were shown to be in excellent agreement with the data. For the DB/DBA samples, the 3D DB corrections were not a clear improvement upon predicted 1D parallaxes. Given that the 3D corrections were for DB white dwarfs only and the samples contained a large fraction of DBA stars, it was concluded that 3D DBA spectroscopic corrections, as well as a re-evaluation of the line broadening parameters (Genest-Beaulieu & Bergeron 2019), are needed to proceed. This will be the subject of a future study.

In this paper, we instead focus on ML2/α calibration at the bottom of the convection zone for 3D DB and DBA models, similar to what has been achieved for 3D DA models (Tremblay et al. 2015). We use a new grid of 3D DBA models consisting of 235 simulations alongside the recently published grid of 47 3D DB models. Our calibration of ML2/α is relevant for the overall thermal and mixing properties of the convection zone. It differs in purpose to the ML2/α calibration based on a detailed spectroscopic analysis performed by Bergeron et al. (2011). This is because the spectral light forming layers for DB and DBA stars are always near or above the top of the convection zone. Additionally, due to the dynamic nature of convection, the mixing length parameter varies throughout the white dwarf structure (Ludwig et al. 1994; Tremblay et al. 2015). Therefore, no single 1D synthetic spectrum at a given ML2/α value can reproduce the entirety of a 3D spectrum (Cukanovaite et al. 2018).

Our calibration is of relevance to many applications. First of all, it is not currently possible to compute 3D evolutionary models of any star. Instead, 1D stellar evolution models have been improved by calibrating the mixing length parameter based on 3D atmospheric models and allowing it to vary accordingly as the star evolves (Trampedach et al. 2014; Magic et al. 2015; Salaris & Cassisi 2015; Mosumgaard et al. 2018; Sonoi et al. 2019). Such calibration has already been performed for DA white dwarfs (Tremblay et al. 2015), but has not been done for DB and DBA stars.

The position of the theoretical blue edge of the instability strip for V777 Her (DBV) white dwarfs is heavily dependent on the assumed convective efficiency at the bottom of the convection zone (Fontaine & Brassard 2008; Córsico et al. 2009; Van Grootel et al. 2017). Larger ML2/α values result in larger $T_{\rm eff}$ of the blue edge. The current empirical blue edge of the strip is defined by PG0112+104 at $T_{\rm eff} \approx 31\,000$ K (at $\log g \approx 7.8$) (Shipman et al. 2002; Provencal et al. 2003; Hermes et al. 2017), approximately 2 000 K higher than the current theoretical blue edge of $T_{\rm eff} \approx 29\,000$ K (at $\log g \approx 7.8$) calculated at the spectroscopically-calibrated ML2/$\alpha = 1.25$ (Van Grootel et al. 2017). This suggests that higher convective efficiency is needed to correctly model the empirical blue edge.

ML2/α calibration at the bottom of the convection zone can also provide more accurate convection zone sizes for DB and DBA white dwarfs. This is needed in order to understand the accretion of planetesimals onto white dwarfs, including the mixing of the different accreted chemical elements within the convection zone and their diffusion at its bottom (or floating in the case of hydrogen). These events are frequent around DB and DBA white dwarfs (Kleinman et al. 2013; Veras 2016) and could explain the origin of hydrogen in DBA stars (Gentile Fusillo et al. 2017). However, for a full 3D description of the accretion-diffusion scenario, convective overshoot must also be accounted for (Kupka et al. 2018; Cunningham et al. 2019), which is outside the scope of the current work.

In Sect. 2 we present the grids of 3D DB and DBA atmospheric models and 1D envelope structures used for the calibration of the ML2/α parameter. Sect. 3 describes the general properties of the 3D convection zones and the differences to 1D convection zones. The calibration method is described in Sect. 4 and results are discussed in Sect. 5. We conclude in Sect. 6.

2 NUMERICAL SETUP

2.1 3D atmospheric models

Using the CO^{5}BOLD radiation-hydrodynamics code (Freytag et al. 2002; Wedemeyer et al. 2004; Freytag et al. 2012; Freytag 2013, 2017), we have calculated 285 3D DB and DBA models with 12 000 K $\lesssim T_{\rm eff} \lesssim$ 34 000 K, $7.5 \leqslant \log g \leqslant 9.0$ and $-10.0 \leqslant \log{\rm (H/He)} \leqslant -2.0$, where $\log{\rm (H/He)}$ is the logarithm of the ratio of the number of hydrogen-to-helium atoms in the atmosphere. Fig. 1 illustrates the atmospheric parameter values of our 3D simulations. Appendix A in the Supplementary Material also lists basic information about the 3D models, including their atmospheric parameters, simulation box sizes, running times and intensity contrasts. For DB models we use $\log{\rm (H/He)} = -10.0$ as this low hydrogen abundance practically describes a pure-helium composition. The abundance range chosen covers the majority of observed hydrogen abundances in DB/DBA samples (Bergeron et al. 2011; Koester & Kepler 2015; Rolland et al. 2018). For all abundances, $\log g = 7.5$ models only extend up to 32 000 K due to convective energy transport being negligible at higher $T_{\rm eff}$ for this particular $\log g$. Currently, there are no known low-mass helium-dominated atmosphere white dwarfs, which would be formed as a consequence of binary evolution (Tremblay et al. 2019; Genest-Beaulieu & Bergeron 2019). Therefore, we do not calculate models with $\log g < 7.5$.

The 3D DB simulations have already been presented in Cukanovaite et al. (2018). The same numerical setup was used to calculate 3D DBA models but with equations of state (EOS) and opacity tables appropriate for the given hydrogen abundance. More detail on the numerical setup can therefore be found in Cukanovaite et al. (2018). In summary, each model is computed using the box-in-a-star CO^{5}BOLD setup (Freytag et al. 2012), where a portion of the atmosphere is modelled in a Cartesian 3D box of typical size 150 × 150 × 150 ($x \times y \times z$) grid points with z being the geometric height pointing towards the exterior of the white dwarf. Each simulation has periodic side boundaries. The top boundary is always open to material and radiative flows, whereas the bottom boundary can be open or closed to convective flows. For most of our models the convection zone sizes are vertically too large to be simulated. In this case the open bottom boundary is used. As the effective temperature increases, the convection zone shrinks until its vertical size becomes small enough to fit within the simulation box. For these models we use closed bottom boundary where the vertical velocity is forced to go to zero at the boundary. For all simulations the top boundary is located at $\log \tau_{\rm R} \lesssim -5.0$, where $\log \tau_{\rm R}$ is the logarithm of the Rosseland optical depth. The bottom boundaries are around $\log \tau_{\rm R} = 3.0$, however, some closed bottom simulations had to be extended deeper to justify the enforcement of zero vertical velocity. In most extreme cases, the models had to be vertically extended to 230 grids points, increasing $\log \tau_{\rm R}$ to around 4.

For a given model the input parameters are an equation of state, an opacity table, $\log g$ and a parameter that controls the $T_{\rm eff}$ of the model. The $T_{\rm eff}$ value is recovered after the simulation is run from the spatially and temporally averaged emergent flux. In the case of open bottom models, the entropy of the inflowing material at the bottom boundary controls the $T_{\rm eff}$. For closed bottom models, the controlling parameter is the radiative flux specified at the bottom. For all abundances we use opacity tables with 10 bins with boundaries at $\log \tau_{\rm R}$ = [99.0, 0.25, 0.0, −0.25, −0.5, −1.0, −1.5, −2.0, −3.0, −4.0, −5.0] based on reference 1D models. We rely on the binning technique as outlined in Nordlund (1982), Ludwig et al. (1994), Vögler et al. (2004) and Cukanovaite et al. (2018). We do not include the far-UV opacities assigned to the [−5.0, −99.0] bin due to interpolation issues as was the case for 3D DB simulations (Cukanovaite et al. 2018). The opacity tables and EOS are based on the 1D models of Bergeron et al. (2011), which include the Stark profiles of neutral helium from Beauchamp et al. (1997) and the free-free absorption coefficient of negative helium ions from John (1994). For DBA models the Stark broadening of Tremblay & Bergeron (2009) is used for hydrogen lines.

The 3D models are spatially- and temporally-averaged in order to extract the relevant atmospheric stratifications, i.e. entropy, temperature, pressure and convective flux as functions of $\log \tau_{\rm R}$. The spatial average is performed over constant geometric height, unlike in Cukanovaite et al. (2018) where the spatial average was done over contours of constant $\log \tau_{\rm R}$. The temporal average is performed over the last quarter of the simulation, i.e. the last quarter of the total run time given in Tabs. A1-A6. We confirm that our models are relaxed by monitoring the total flux at all depths and the convergence of the velocity field (Cukanovaite et al. 2018). Relaxation usually occurs in the first half of the simulation, as we start from a simulation that is already close to the final solution.

2.2 1D envelope models

In order to find a mixing length value that best matches the nature of 3D convection zones, we use the updated 1D DB and DBA envelope models of Van Grootel et al. (2017) and Fontaine et al. (2001), which span the same parameter range as our 3D atmospheric models but also different values of ML2/α, namely $0.4 \leqslant {\rm ML2}/\alpha \leqslant 1.4$ in steps of 0.1. The envelopes rely on non-grey upper boundary conditions extracted from the atmospheric models of Bergeron et al. (2011), and on the non-ideal EOS of Saumon et al. (1995). Turbulent pressure is not included in the envelope structures.

For the majority of 3D models the inflowing entropy at the base of the convection zone (the input parameter for open bottom models which controls $T_{\rm eff}$ of the model) is used for ML2/α calibration. In order to have a common entropy zero-point between the 1D envelopes and 3D atmospheres, we re-calculate the 1D entropy from temperature and pressure at the base of the 1D envelope convection zone. The entropy is re-calculated with and without partial degeneracy to demonstrate the degeneracy effects. Fig. 2 shows entropy as a function of $T_{\rm eff}$ for selected models. At high $T_{\rm eff}$ the partial degeneracy is negligible as the chemical potential of free electrons has a large negative value. Partial degeneracy becomes important for cool $T_{\rm eff}$ models due to their low temperatures and high densities. For the $\log{\rm (H/He)} = -10.0$

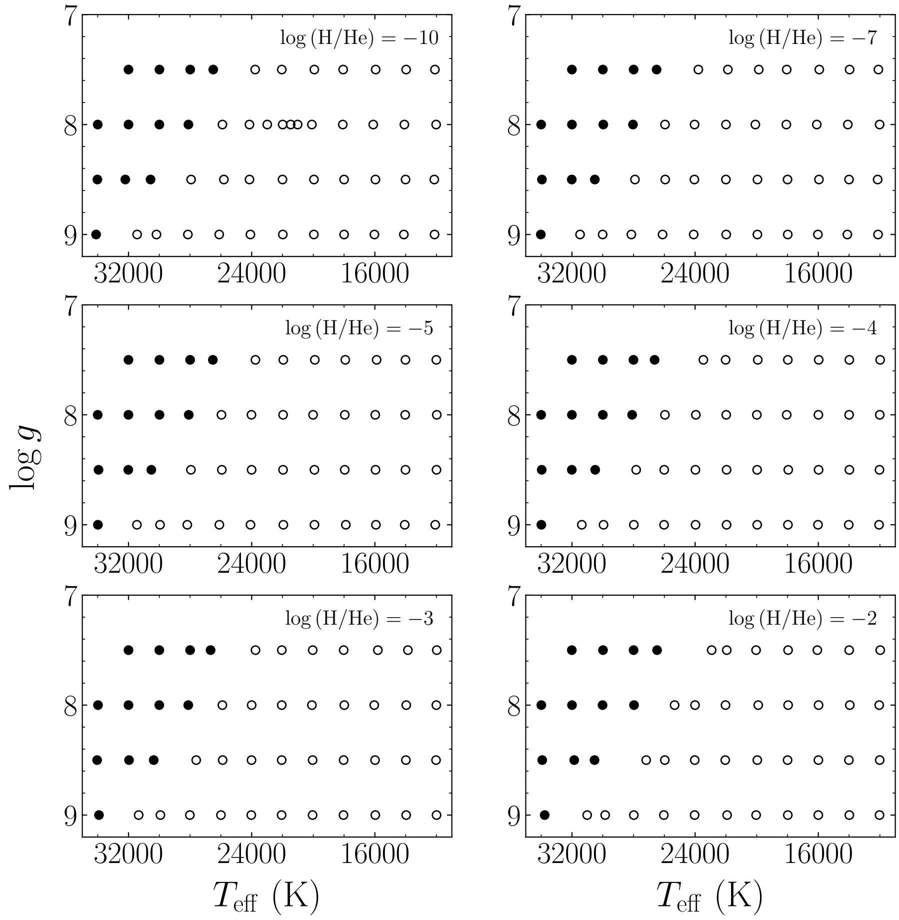

Figure 1. The abundances, surface gravities and effective temperatures of the 3D models presented in this paper. Open and filled circles denote the models with open and closed bottom boundaries, respectively.

grid, our first-order partial degeneracy correction begins to break down for the lowest $T_{\rm eff}$ models not plotted in Fig. 2, namely $T_{\rm eff} \lesssim 14\,000$, 14 000, 16 000, 18 000 K for $\log g = 7.5$, 8.0, 8.5, 9.0 models, respectively. Similar behaviour is observed for the DBA grid. Below these $T_{\rm eff}$ convection in envelopes is almost fully adiabatic everywhere and becomes independent of the particular choice of ML2/α. Therefore, we do not attempt calibration of ML2/α in that particular $T_{\rm eff}$ regime (see Sect. 4). We find that partial degeneracy is more important for low $T_{\rm eff}$ DB/DBA models than low $T_{\rm eff}$ DA models (see Fig. 1 of Tremblay et al. 2015) possibly due to the higher densities of DB models.

From 1D envelopes we also extract the ratio $\log(M_{\rm CVZ}/M_{\rm tot})$, where $M_{\rm CVZ}$ is the mass of the convection zone integrated from the surface of the white dwarf to the bottom of the convection zone and $M_{\rm tot}$ is the total mass of the white dwarf. An example of this is shown in Fig. 3. As expected, varying the value of the ML2/α parameter for models where superadiabatic convection is important has a significant effect on the mass of the convection zone. The change can be as much as ≈ 4 dex for $\log g = 7.5$ DB and DBA models and ≈ 3 dex for $\log g = 9.0$ models. By calibrating ML2/α with our 3D models (see Sect. 4) we can narrow down the uncertainty on the mixed mass within the convection zone.

The convection zone size increases with decreasing $\log g$ and decreasing $T_{\rm eff}$ (Fontaine & van Horn 1976). Shallower convection zones are expected for DBA models as the presence of hydrogen increases the total opacity, decreasing the atmospheric density and pressure (Fontaine & van Horn 1976). This is also seen for late-type stars with increased metallicity (Magic et al. 2013). The decrease in density and pressure results in higher adiabatic entropy (see Sec. 3), and therefore lower convective efficiency (and entropy jump, see Sec. 5.1) and smaller convection zones (Magic et al. 2013). Fig. 4 shows $\log(M_{\rm CVZ}/M_{\rm tot})$ for the $\log({\rm H/He}) = -2.0$ grid. By comparing Figs. 3 and 4 it is clear that the presence of hydrogen does indeed shrink the convection zones.

3 THE CONVECTION ZONE

The envelopes of cool DA and DB white dwarfs are convective, with the top of the convection zone almost perfectly overlapping with the photospheric layers (Tassoul et al. 1990), meaning that convection is essential for modelling both atmospheres and envelopes of cool white dwarfs. In 1D atmospheric and envelope models the convective layers are defined by the Schwarzschild criterion

$$\left(\frac{\partial \ln T}{\partial \ln P}\right)_{\rm radiative} > \left(\frac{\partial \ln T}{\partial \ln P}\right)_{\rm adiabatic}, \quad (2)$$

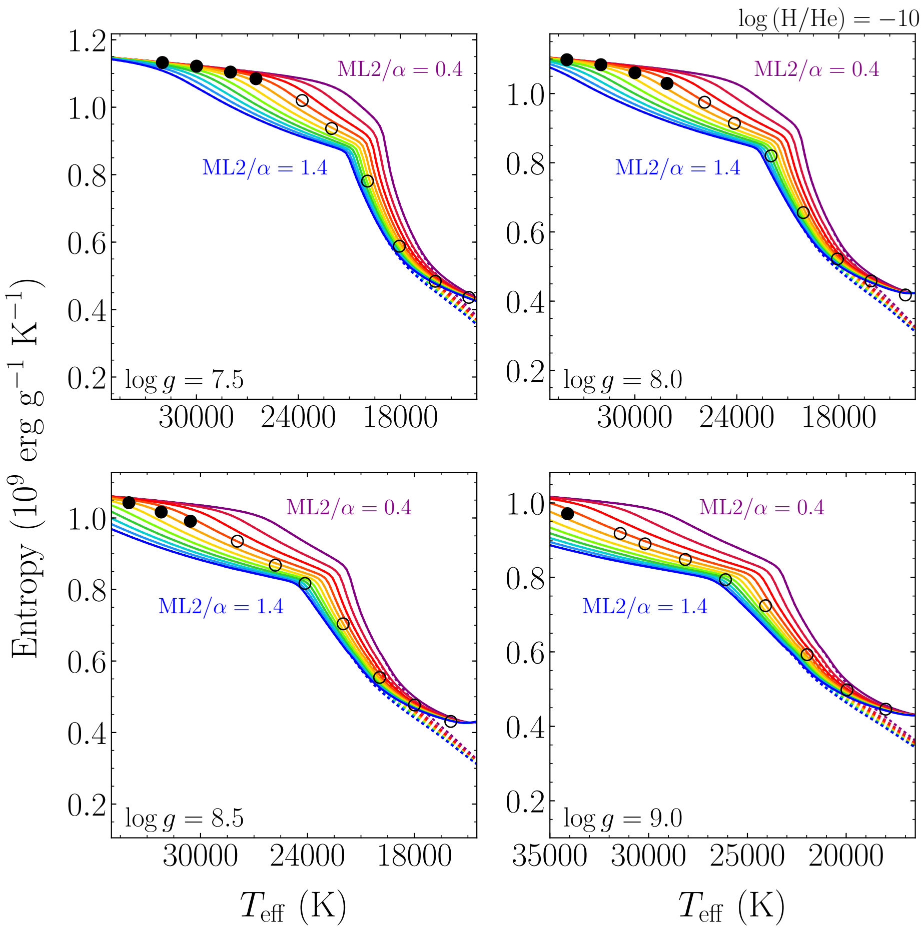

Figure 2. The entropy at the bottom of the convection zone defined by the Schwarzschild criterion as a function of $T_{\rm eff}$ for 3D DB open (open circles) and closed (filled circles) bottom models, and for 1D DB envelopes with different values of the mixing length parameter. The ML2/α value decreases by increments of 0.1 from the dark blue line (ML2/α = 1.4) all the way up to the dark purple line (ML2/α = 0.4). We show the 1D entropies with (solid lines) and without (dashed lines) partial degeneracy effects taken into account. The $\log g$ values of the models are indicated on the panels.

where T and P are the temperature and pressure. Therefore, only those layers that locally satisfy this inequality are able to transport energy through convection, leading to abrupt and clearly-defined boundaries of the convection zone in 1D. This is a limited approximation of the turbulent nature of convection, which is better explored with the use of 3D models. There are at least two ways one can define convection zone boundaries and subsequently convection zone sizes in 3D simulations. In the following we use the Schwarzschild criterion (the Schwarzschild boundary) and the zero convective flux (the flux boundary) definitions.

The Schwarzschild criterion can be rewritten in terms of the entropy gradient with respect to $\log \tau_{\rm R}$, such that the convective layers are defined by

$$\frac{{\rm d}s}{{\rm d}\tau_{\rm R}} > 0\,, \qquad (3)$$

where s is the entropy. We use this definition to determine the edges of the convection zone in both 1D and $\langle$3D$\rangle$ entropy stratifications, focusing on the bottom boundary, defining it to be the Schwarzschild boundary.

Unlike in the 1D case, the 3D convective energy is transported even beyond the Schwarzschild boundary. This is due to the acceleration of the overdense convective downdrafts in the layers just above the base of the convection zone. In response, because of mass conservation warm material is transported upwards, resulting in a positive convective flux (Tremblay et al. 2015). We define the flux boundary to be the region where the ratio of convective-to-total flux goes to zero. The convective flux, $F_{\rm conv}$, is calculated using

$$F_{\rm conv} = \left\langle \left(e_{\rm int} + \frac{P}{\rho} \right) \rho u_z \right\rangle + \left\langle \frac{\mathbf{u}^2}{2} \rho u_z \right\rangle - e_{\rm tot} \langle \rho u_z \rangle, \qquad (4)$$

where $e_{\rm int}$ is the internal energy per gram, ρ is the density, u_z is the vertical velocity, $\mathbf{u}$ is the velocity vector and $e_{\rm tot}$ is the total energy, defined as

$$e_{\rm tot} = \frac{\langle \rho e_{\rm int} + P + \rho \frac{\mathbf{u}^2}{2} \rangle}{\langle \rho \rangle}. \qquad (5)$$

The first term of Eq. 4 is the enthalpy flux, the second term is the kinetic energy flux and the third term is the mass flux weighted energy flux, which is subtracted in order to correct for any non-zero mass flux arising in the numerical simulations. This definition is identical to the one used in Tremblay et al. (2015). Some authors, for instance Cattaneo et al. (1991) and Canuto (2007), have referred to the sum of

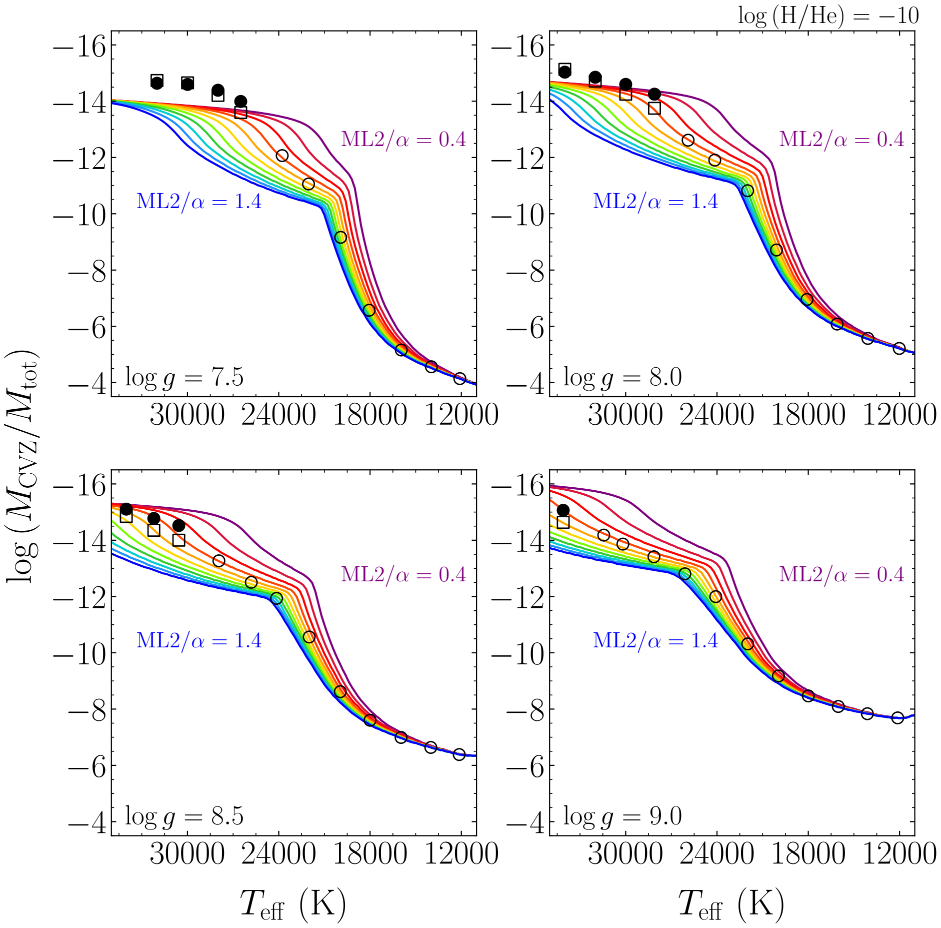

Figure 3. The fraction of the convection zone mass to the total mass of the white dwarf as a function of $T_{\rm eff}$ for 3D DB models and 1D DB envelopes (solid lines) with different values of the mixing length parameter. The ML2/α value decreases by increments of 0.1 from the dark blue line (ML2/α = 1.4) all the way up to the dark purple line (ML2/α = 0.4). The Schwarzschild boundaries for the 3D open bottom models are indicated by open circles; filled circles represent the Schwarzschild boundary for closed bottom 3D models; open squares represent the flux boundary for closed bottom 3D models.

enthalpy and kinetic energy flux as "convected" flux. In general, convective flux is a synonym for enthalpy flux only. By adding kinetic energy flux, the "convective flux" boundary is moved closer to the Schwarzschild boundary, as kinetic energy is always negative for simulations presented here, which have standard granulation topology of slow and broad upflows surrounded by fast and narrow downflows. Therefore, ML2/α values calibrated based on the enthalpy and kinetic flux boundary will be smaller than the calibrated values based on enthalpy flux alone (Kupka et al. 2018; Tremblay et al. 2015). As shown by Kupka et al. (2018) the boundary associated with the enthalpy flux indicates where downflows become hotter than their surroundings, which is related to buoyancy, the driving mechanism of convection. Therefore, the definition of convective flux based on enthalpy flux would be crucial in studies of downflows. However, for consistency with previous work of Tremblay et al. (2015) we use the definition of "convective" flux as defined in Eq. 4. In MLT, convective flux refers to enthalpy flux only, as kinetic flux is zero everywhere.

Figs. 5 and 6 demonstrate the Schwarzschild and flux boundaries, respectively. In the case of helium-dominated atmosphere white dwarfs, at higher $T_{\rm eff}$ there are two convectively-unstable regions related to He I and He II ionization. These zones can either be separated by a convectively stable region or merge into one convection zone depending on the $T_{\rm eff}$. This can also happen for a model at the same $T_{\rm eff}$, but for different definitions of the convection zone as shown in Figs. 5 and 6, where the model at $T_{\rm eff} \approx 28\,000$ K has two clearly defined and separated convectively-unstable regions in terms of the Schwarzschild criterion, yet in terms of the flux criterion the two helium zones are indistinguishable, since the flux boundary penetrates deeper. At the highest $T_{\rm eff}$ only the He II convection zone remains as He I is fully ionised.

In Fig. 6 we see a region beyond the flux boundary where the ratio of convective-to-total flux becomes negative. This is the convective overshoot region, where the negative convective flux is due to the convective downflow plumes being warmer than the surroundings (Zahn 1991; Tremblay et al. 2015). There is no equivalent region in 1D models and therefore we do not attempt to calibrate the mixing length in any form to describe this region. However, overshoot is important for convective mixing studies. For DA white dwarfs it has been shown that more material can be mixed in the convection zone even beyond the negative flux region (the

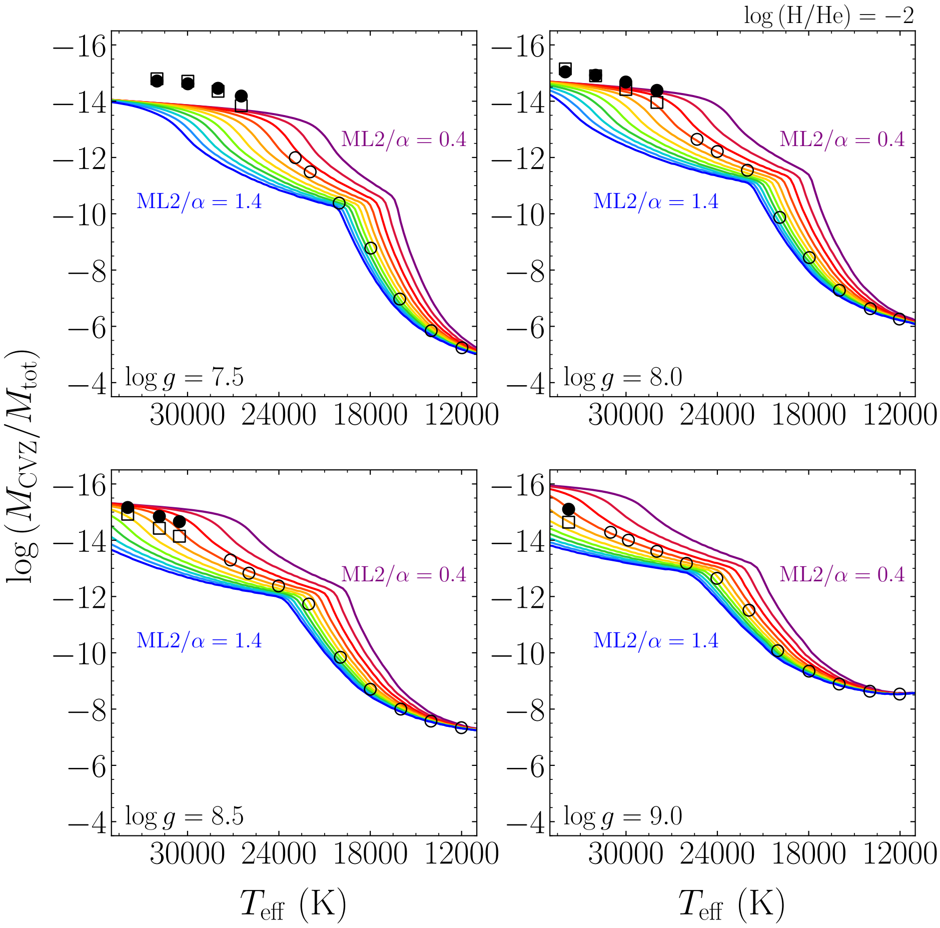

Figure 4. Same as Fig. 3, but for a DBA grid with $\log(\mathrm{H/He}) = -2.0$.

velocity overshoot region), impacting the mass, abundances, and diffusion times of accreted metals (Freytag et al. 1996; Koester 2009; Kupka et al. 2018; Cunningham et al. 2019). This is still unexplored for helium-rich atmospheres.

4 THE CALIBRATION METHOD

4.1 Closed bottom models

For the closed bottom 3D models (examples shown in Figs. 5 and 6) both the Schwarzschild and flux boundaries can be directly probed and the ⟨3D⟩ temperature and pressure values at the two boundaries can be extracted. Similarly, from 1D envelope structures we also have access to the temperature and pressure at the bottom of the 1D Schwarzschild boundary. These quantities are displayed in Figs. 7 and 8.

For each 3D model with given atmospheric parameters, we interpolate over 1D envelopes with the same atmospheric parameters but varying values of ML2/α, in order to find the ML2/α value that gives the same temperature and pressure at the base of either Schwarzschild or flux boundary of the 3D convection zone. We refer to these calibrated ML2/α values as ML2/α_{S} and ML2/α_{f} for Schwarzschild and flux boundaries, respectively. The calibrated ML2/α parameters between temperature and pressure generally agree within ≈ 0.05 even in the most extreme cases such as $\log g = 9.0$ shown in Figs. 7 and 8. Therefore, we take an average of the two ML2/α values. This gives us an indication of the average temperature gradient in the vicinity of the base of the convection zone.

A larger ML2/α value means that the convection zone extends deeper into the envelope and thus both the temperature and pressure are larger at the base. As T_{eff} increases for $\log g = 7.5$ and 8.0 models, the different ML2/α envelopes start to converge, yet we can still deduce that the calibrated ML2/α value in this T_{eff} range must be on the lower end of our ML2/α range, meaning that the convective efficiency is very low.

The blue edge of the DBV instability strip is thought to be related to recombination of the main constituent of the atmosphere, which also causes convection to set in. Our 3D models indicate that a lower ML2/α value than 1.25 (the value used by Van Grootel et al. (2017) to determine the theoretical blue edge) best represents the base of the convection zone both for Schwarzschild and flux boundaries. In general, with the lowering of ML2/α value, convection will occur later in the white dwarf's evolution (i.e. at lower T_{eff}).

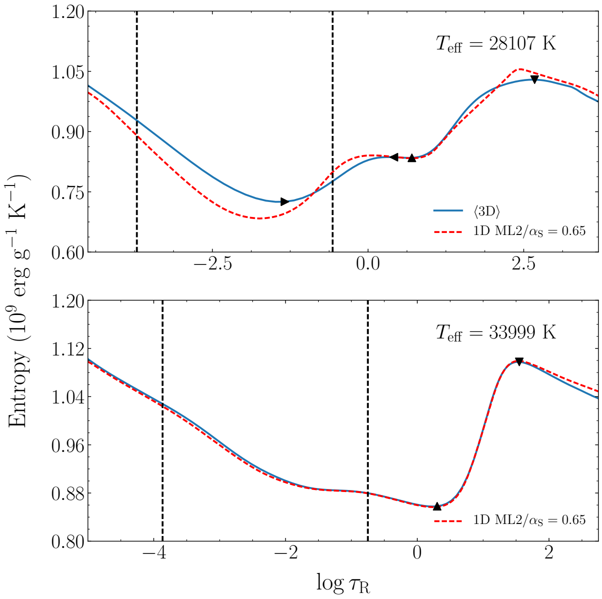

Figure 5. Entropy stratifications of two 3D closed bottom models with $\log g = 8.0$ and $\log(\mathrm{H/He}) = -10.0$ are shown as solid blue lines. The dashed black lines indicate the flux-forming region for wavelengths 3500 Å to 7200 Å, representing the atmosphere of the white dwarf in terms of visible light. 1D models calculated at calibrated ML2/$\alpha_{\rm S}$ are shown as dashed red lines. According to the Schwarzschild criterion, at $T_{\rm eff} \approx 28\,000$ K there are two convectively unstable regions due to He I and He II ionization. The top and bottom of the first convective region is denoted by right- and left-pointing triangles, respectively. The second convective region is indicated by upward- and downward-pointing triangles. The two convective regions are separated by a small region which is convectively stable in terms of the Schwarzschild criterion. At $T_{\rm eff} \approx 34\,000$ K, according to the Schwarzschild criterion there is only one convective region (He II) left, which is denoted by the upward- and downward-pointing triangles.

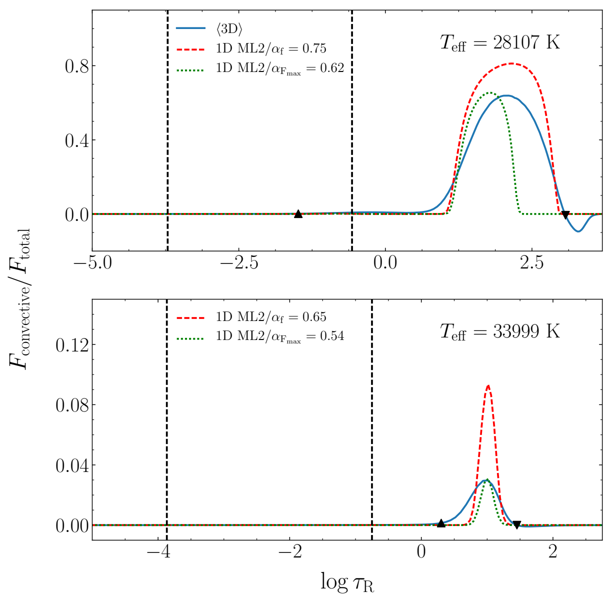

Figure 6. The ratio of the convective-to-total flux as a function of the $\log \tau_{\rm R}$ for two 3D closed bottom $\log g = 8.0$, $\log(\mathrm{H/He}) = -10.0$ models is shown in solid blue. The upward- and downward-pointing triangles denote the top and bottom flux boundaries of the convection zone, respectively. The dashed black lines represent the flux-forming region for wavelengths 3500 Å to 7200 Å. Red dashed lines show the 1D models calculated at calibrated ML2/$\alpha_{\rm f}$, and green dotted lines show 1D models calculated at ML2/$\alpha_{\rm F_{max}}$ (see Sect. 5.2). Unlike the Schwarzschild boundary, at $T_{\rm eff} \approx 28\,000$ K the two convectively-unstable regions are inseparable in terms of the flux due to the dynamics of the downdrafts. Beyond the flux boundary, a region of negative flux related to convective overshoot is observed.

The theoretical location of the blue edge of the instability strip should therefore be at a lower $T_{\rm eff}$ than predicted by current studies.

With closed bottom models we can also directly calculate $\log(M_{\rm CVZ}/M_{\rm tot})$ for either convection zone boundary. In Figs. 3 and 4 we compare 3D $\log(M_{\rm CVZ}/M_{\rm tot})$ to the predictions of 1D envelopes. Unlike the DA case (Tremblay et al. 2015) we do not find that mass-calibrated ML2/α values are similar to the temperature- and pressure-calibrated ML2/α values. As the mass is calculated independently of either temperature or pressure, a disagreement is not unexpected since 1D models cannot reproduce all of the dynamic quantities of 3D models. This is clearly shown in Figs. 5 and 6, where we plot ⟨3D⟩ structures and corresponding 1D atmospheric models of Bergeron et al. (2011) calculated at calibrated ML2/$\alpha_{\rm S}$ and ML2/$\alpha_{\rm f}$ values, respectively. As expected, the ⟨3D⟩ and 1D structures agree in the vicinity of either boundary, but the overall 1D and ⟨3D⟩ structures do not agree well. For all closed bottom models at $\log g = 7.5$ and 8.0, the masses included in the 3D convection zones diverge off the 1D envelope predictions, such that they are much smaller than what is possible to achieve in 1D within our range of ML2/α values.

In Figs. 3 and 4 flux and Schwarzschild boundary reversal is observed, just like in 3D DA models. As mentioned previously, the reversal is due to kinetic energy flux and if neglected it is not observed (Kupka et al. 2018; Tremblay et al. 2015). Such reversal does not occur in 1D models, as kinetic energy flux is not considered.

For studies in need of the physical conditions near the base of the convection zone, the calibrations shown in Figs 7 and 8 and listed in Tabs. A13 to A18 of Appendix A should be used. The masses listed in those tables are the 1D convection zone masses found from 1D envelopes calculated at 3D calibrated ML2/α values. For studies where such approximations are not adequate, the direct use of 3D structures would be more beneficial.

4.2 Open bottom models

For open bottom models we are unable to probe the bottom of the convection zone as our simulations are not deep enough. We can, however, exploit the fact that in 3D models a fraction of upflows from the bottom of the deep convection zone retain their adiabatic entropy almost all the way up to the observable atmospheric layers by not interacting with neighbouring downflows via heat exchange (Stein & Nordlund 1989). This means that the spatially- and temporally-resolved entropy has a plateau corresponding to this adiabatic entropy value and it can be used to calibrate ML2/α (Steffen 1993; Ludwig et al. 1999). Example entropy

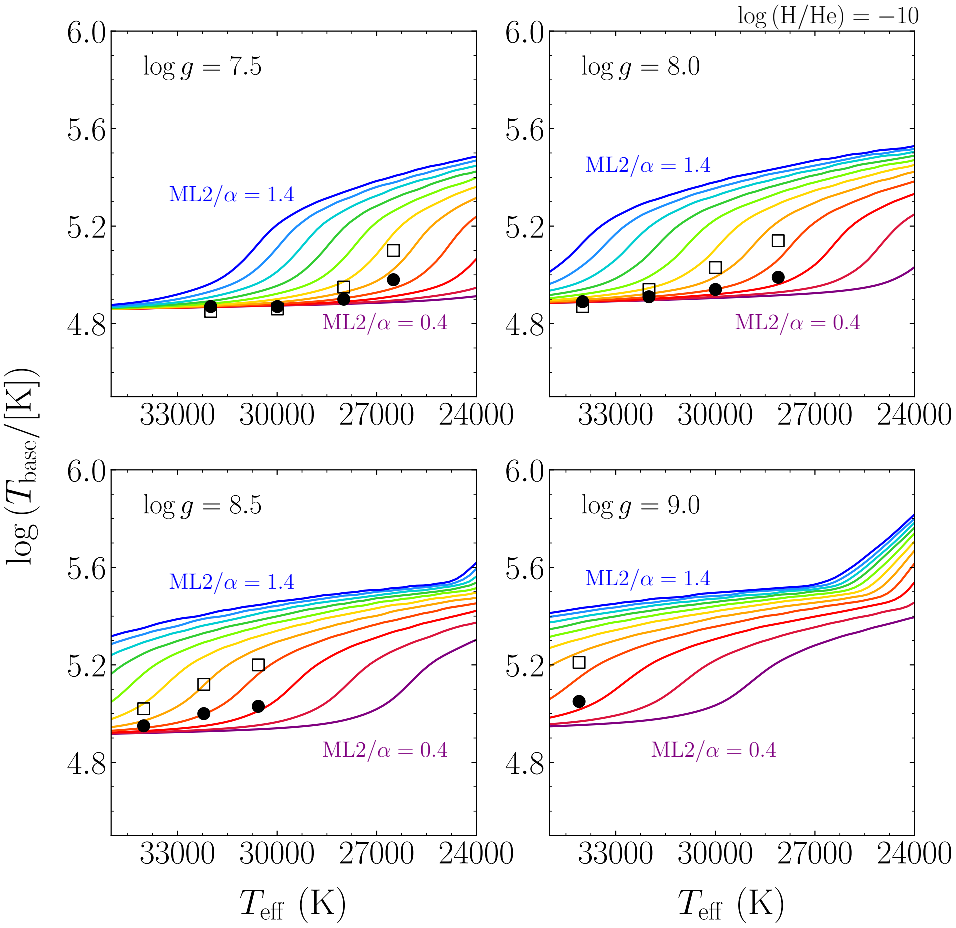

Figure 7. The logarithm of the temperature at the base of the convection zone as a function of $T_{\rm eff}$ for DB white dwarfs. The solid lines are 1D envelope temperatures at the Schwarzschild boundary for varying ML2/α values. The ML2/α value decreases by increments of 0.1 from the dark blue line (ML2/α = 1.4) all the way down to the dark purple line (ML2/α = 0.4). The solid circles represent the temperature of closed bottom 3D models at the Schwarzschild boundary, the open squares are the temperatures of closed bottom 3D models at the flux boundary. The $\log g$ values are indicated on the plots.

plateaus are shown in Fig. 9 for $\log$ (H/He) = −10.0 and $\log$ (H/He) = −2.0 models, where we also plot the temporally- and horizontally-averaged entropy stratifications. The averaged entropy is lower and does not reach the adiabatic entropy as it also considers the small entropy of the downflows. For CO^{5}BOLD the adiabatic entropy value is the inflowing entropy input parameter and an entropy plateau is observed in all open bottom simulations.

For each 3D model with given atmospheric parameters, we interpolate over the different ML2/α 1D envelopes with the same atmospheric parameters to find the 1D entropy at the bottom of the Schwarzschild boundary that best matches the 3D adiabatic entropy. We show this in Fig. 2. The entropy of closed bottom models is also shown, but for these models we do not use the entropy to calibrate. This is because we have already calibrated ML2/α directly in Sec. 4.1 and generally for closed bottom models the upflows are not adiabatic in any portion of the convection zone.

The adiabatic entropy value is for the 3D Schwarzschild boundary only. We cannot access the flux boundary for open bottom models. Instead, we use the results from closed bottom models to estimate the ML2/α value that best represents the flux boundary for open bottom models. For closed bottom models that do not show the flux and Schwarzschild boundary reversal we find the relation ML2/$\alpha_{\rm f}$= 1.17 ML2/$\alpha_{\rm S}$ with a standard deviation of around 3%. A similar result of ML2/$\alpha_{\rm f}$= 1.16 ML2/$\alpha_{\rm S}$ with a standard deviation of around 3% was found for 3D DA models (Tremblay et al. 2015).

In Figs. 3 and 4 we show the $\log (M_{\rm CVZ}/M_{\rm tot})$ value for both open and closed bottom models with $\log$ (H/He) = −10.0 and −2.0, respectively. Unlike the closed bottom case, we cannot directly access the bottom of either convection zone boundary for open bottom models. Thus, the masses for open bottom 3D models are extracted from the 1D envelopes with ML2/α value that best matches the 3D adiabatic entropy.

As mentioned earlier and shown in Fig. 2, at the lowest $T_{\rm eff}$ the different ML2/α value envelopes converge to the same solution as convection becomes adiabatic and insensitive to ML2/α even in the upper atmosphere. In these cases, the derived mass fraction does not change significantly between the different values of the ML2/α parameter. Therefore, we propose not to interpolate for the best matching mixing length parameter, but to set it to 1.0 for both Schwarzschild and flux boundaries.

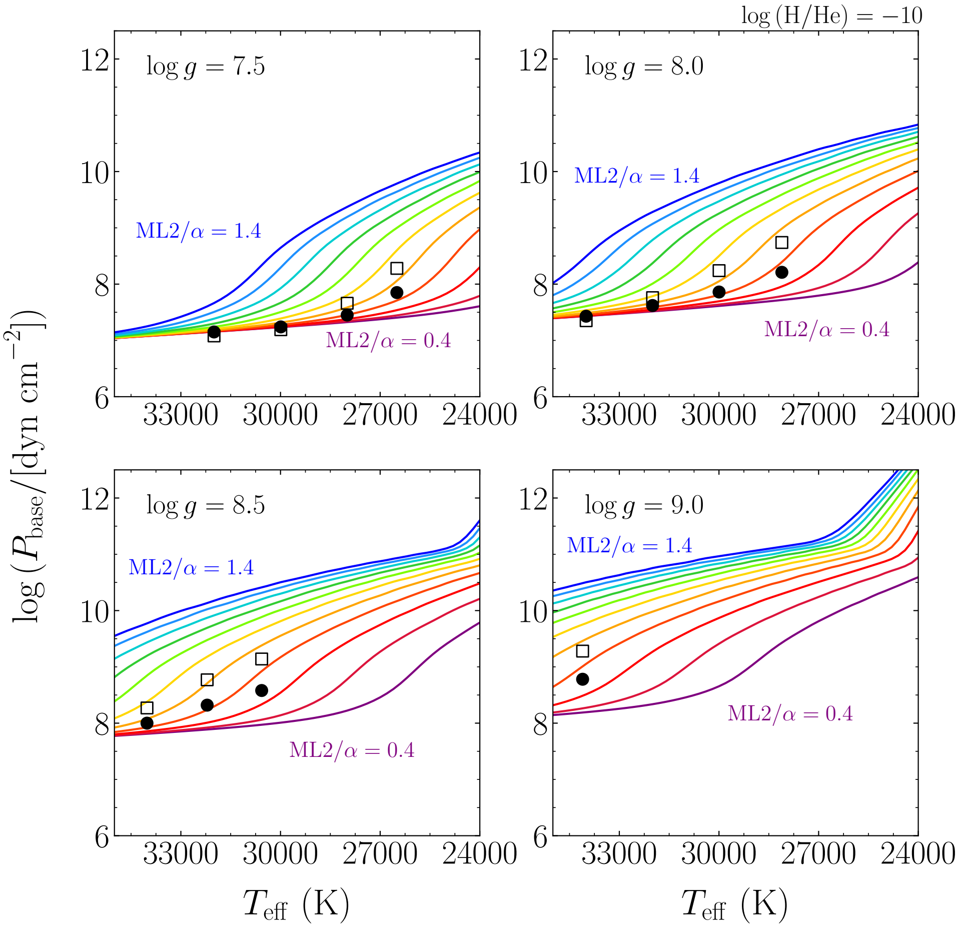

Figure 8. Similar to Fig. 7 but for pressure at the base of the convection zone.

5 DISCUSSION

The calibrated ML2/α values are shown in Figs. 10 and 11 for the Schwarzschild and flux boundaries, respectively, and in the Appendix A of the Supplementary Material. In all cases, ML2/α values are smaller than what is often used in evolutionary models, i.e. ML2/α = 1.25. This means that 3D models predict lower convective efficiencies. Given that the value of 1.25 is based on matching observed and model spectra and therefore describes the convective efficiency in the photosphere, it is not unexpected that it is different to the convective efficiency at the bottom of the convection zone. Interestingly, the mean convective efficiency for DB/DBA white dwarfs is very similar, or only slightly larger, to that of DA stars (Tremblay et al. 2015).

The plateaus observed at low $T_{\rm eff}$ are artificial. They are the consequence of fixing the value of ML2/$\alpha_{\rm S}$ = ML2/$\alpha_{\rm f}$= 1.0 for $T_{\rm eff}$ where the structures become insensitive to the ML2/α parameter. A similar effect can be observed at the highest $T_{\rm eff}$, where the calibration is forced to values of 0.65 for both ML2/$\alpha_{\rm S}$ and ML2/$\alpha_{\rm f}$, as none of the 1D ML2/α values can reproduce the boundaries of the 3D convection zone. Since the convective zone is in any case very small and inefficient in this regime, the fixed value may not be a concern for some applications. If on the other hand detailed convective properties are required, it is more appropriate to directly use 3D models which also include velocity overshoot (see Sect. 5.3).

The peaks observed in Figs. 10 and 11 which seem to shift to higher $T_{\rm eff}$ for higher $\log g$, are associated with the knee-like feature of the 1D envelopes seen in Figs. 2, 3 and 4, which we suggest is related to the disappearance of the He II convection zone as the white dwarf evolves to lower $T_{\rm eff}$. This transition is different in 3D, potentially because of the non-local coupling of the two convection zones. The knee-feature also means that ML2/α calibration is more sensitive in that region.

5.1 Calibration of the entropy jump

Studies such as Magic et al. (2015) have also performed ML2/α calibrations for solar-like stars based on the entropy jump associated with superadiabatic convection. Examples of such entropy jumps can be seen in Figs. 5 and 9 for closed and open bottom models, respectively. In their calibration, Magic et al. (2015) define the jump as the difference between the constant entropy value of the adiabatic convection zone and the entropy minimum for both 1D and 3D models. We use a similar method to investigate more clearly the variations of ML2/α as a function of $T_{\rm eff}$.

To perform the calibration we do not use the evolution-

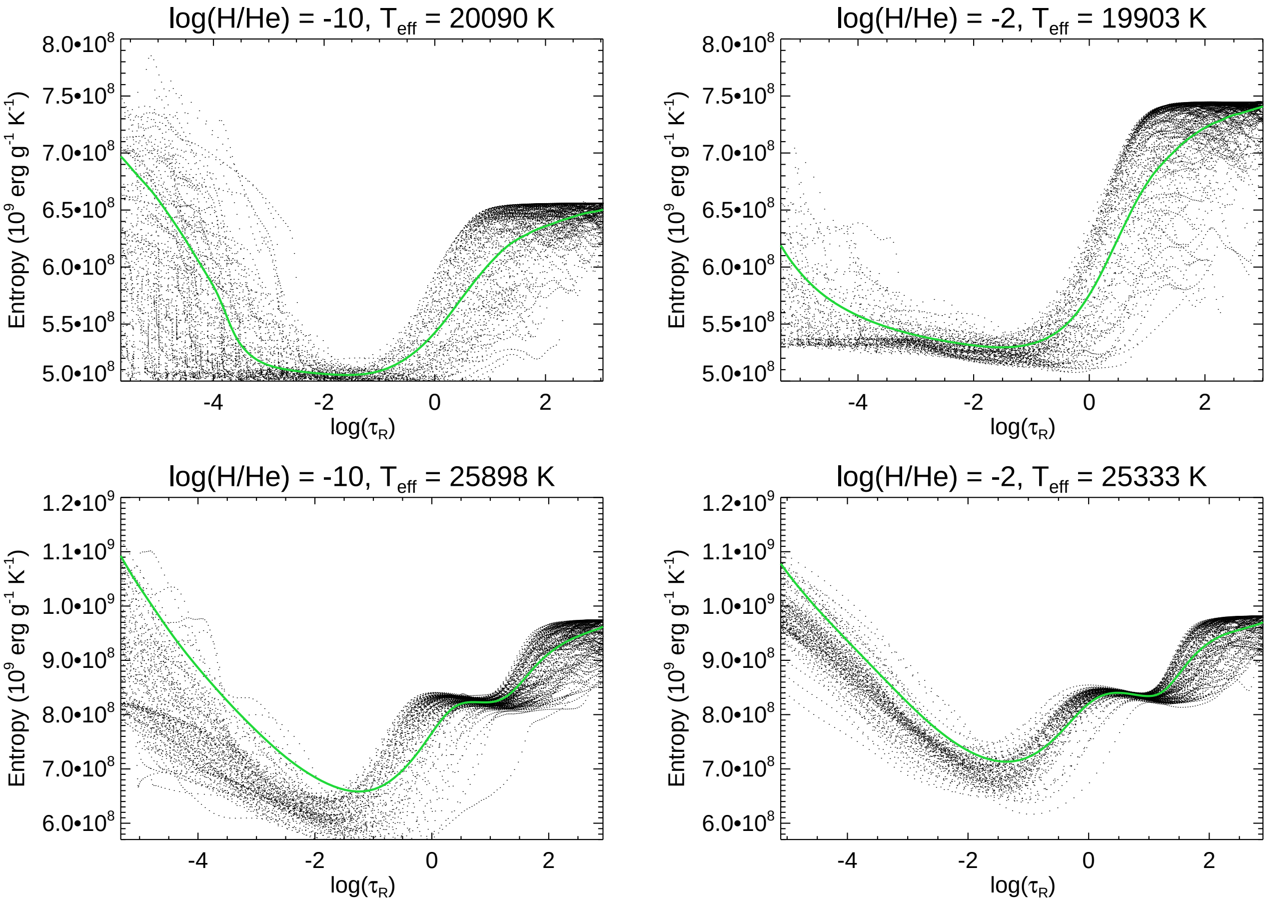

Figure 9. The spatially- and temporally- resolved entropy of $\log g = 8.0$ 3D open bottom models. The top two plots show the entropy stratification when only the He I convection is present, whereas the bottom two panels show models with both He I and He II convection zones. In green we plot the averaged entropy over constant geometric depth and time. Although the average entropy does not reach the adiabatic value near the bottom of the simulation, it is clear that the spatially- and temporally- resolved entropy has a plateau at deeper layers, which corresponds to the inflowing entropy, an input parameter of our 3D models.

ary models presented in Sec. 2.2. Instead, we use the 1D atmospheric models of Bergeron et al. (2011). This grid of models spans the same range of atmospheric parameters as our 3D and 1D envelope grids, but also ML2/α values in the range $0.5 \leqslant$ ML2/$\alpha \leqslant 1.5$ in steps of 0.25. We define the entropy jump, $s_{\rm jump}$, as

$$s_{\rm jump} = s(\log \tau_{\rm R} = 2) - s_{\rm min}, \qquad (6)$$

where $s(\log \tau_{\rm R} = 2)$ is the entropy at $\log \tau_{\rm R} = 2$ and $s_{\rm min}$ is the minimum entropy value. In the 3D case, the entropy stratification is temporally- and spatially-averaged, with the spatial average being performed over constant geometric height as before. We calculate $s_{\rm jump}$ both for the 3D atmospheric models, and for 1D atmospheric models calculated at different values of ML2/α. We then find the value of ML2/α, which we refer to as ML2/$\alpha_{s_{\rm jump}}$, that best represents the given $\langle$3D$\rangle$ entropy jump. In late-type stars, the entropy jump was found to decrease for increasing values of ML2/α (Magic et al. 2015). This is because as convection becomes more efficient, smaller temperature gradients in the superadiabatic layers are needed to transport the same flux (Sonoi et al. 2019). This relation holds for DB and DBA 1D models where the entropy minimum is located at the top of the He I convection zone (see Fig. 9 for example). It breaks down when the He I convection zone disappears or when the entropy minimum moves to the top of the He II convection zone. This happens for the majority of 3D closed bottom models, and therefore we only perform ML2/$\alpha_{s_{\rm jump}}$ calibration for 3D open bottom models.

We show the ML2/$\alpha_{s_{\rm jump}}$ values for DB white dwarfs in Fig. 12. Similar results were found for DBA white dwarfs. For all $\log g$ apart from 7.5, the peaks observed in ML2/$\alpha_{s_{\rm jump}}$ are at the same $T_{\rm eff}$ as the peaks observed for ML2/$\alpha_{\rm S}$ and ML2/$\alpha_{\rm f}$. By looking at the structures directly, the peaks are clearly associated with the disappearance of the second-hump in the entropy profile due to He II convection zone as the white dwarf cools to lower $T_{\rm eff}$. Examples of double peaked entropy profiles are shown in Fig. 9.

For atmospheric parameters where convection is sensitive to the ML2/α value (e.g. the calibrated value of ML2/α is not fixed in Figs. 10 and 11), we find reasonable agreement between the ML2/$\alpha_{s_{\rm jump}}$, ML2/$\alpha_{\rm S}$ and ML2/$\alpha_{\rm f}$ calibrations.

Magic et al. (2015) found that their ML2/α values based on the entropy jump were higher than the ML2/α values based on the adiabatic entropy (ML2/$\alpha_{\rm S}$). They attribute this to the 1D entropy minimum being lower than

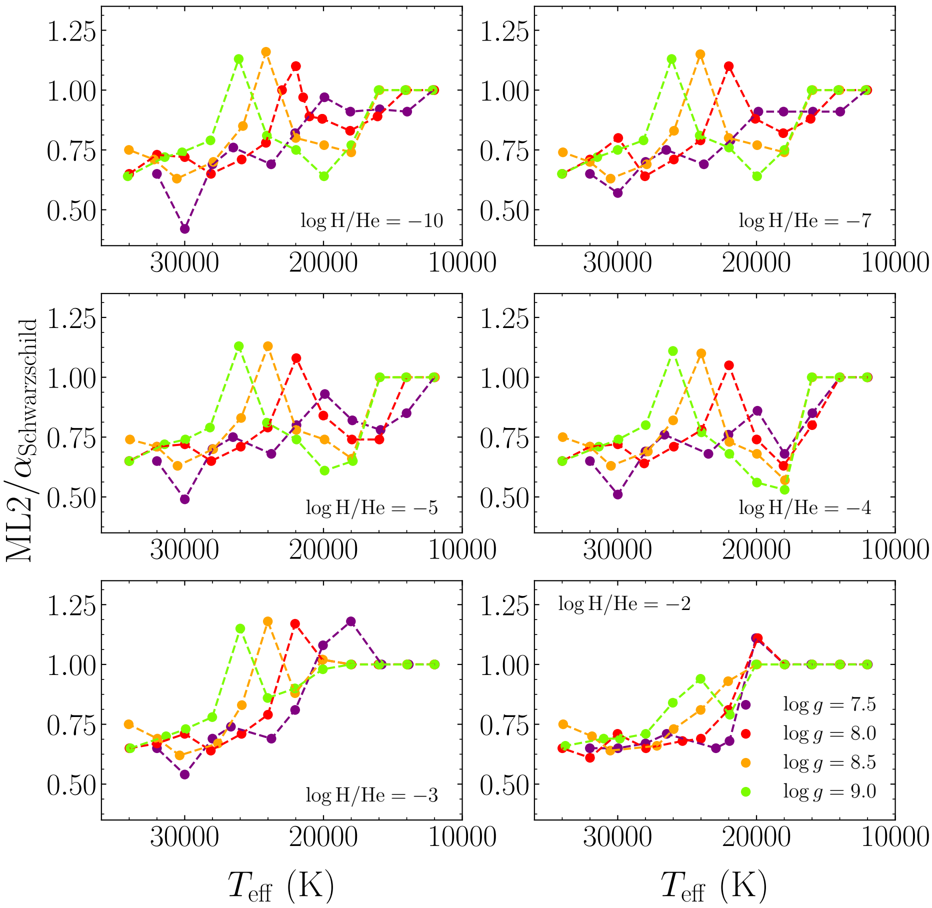

Figure 10. The calibrated mixing length parameter based on the Schwarzschild boundary is plotted as solid colour points which are connected for clarity for the same surface gravity. The value of $\log(\mathrm{H/He})$ is indicated on each panel.

the ⟨3D⟩ entropy minimum, which is also the case for our lower $T_{\rm eff}$ models. This explains why at low $T_{\rm eff}$ we find ML2/$\alpha_{\rm S}$ and ML2/$\alpha_{\rm f}$ values that are larger than the value of ML2/$\alpha_{\rm S_{jump}}$ (for example, $T_{\rm eff} \lesssim 20\,000$ K for $\log g$ = 8.0 DB models).

From the studies of ML2/$\alpha_{\rm S_{jump}}$, ML2/$\alpha_{\rm S}$ and ML2/$\alpha_{\rm f}$ it is apparent that the peaks in ML2/α values are observed close to the red edge of the DBV instability region. This means that in terms of the 3D picture, the mixing length changes quite rapidly in the region where pulsations are empirically observed to stop. As current DBV studies use an ML2/α value of 1.25, and the peak is closer to this value than the calibrated ML2/α values at other $T_{\rm eff}$, we expect that our calibration will not significantly alter the current theoretical DBV studies at the red edge of the instability strip.

5.2 Calibration of the maximum convective flux

An alternative way to calibrate the ML2/α values for closed bottom models has been proposed by Tremblay et al. (2015). The calibration is based on the maximum value of the convective-to-total flux. This better represents the total amount of energy transported by convection as shown for DA white dwarfs by Tremblay et al. (2015). We perform this calibration for DB and DBA closed bottom models using the 1D atmospheric models of Bergeron et al. (2011), i.e. same grid that was used in Sec. 5.1, but with additional grids at ML2/α = 0.55, 0.60, 0.65 and 0.70 as convective flux changes significantly with ML2/α value. Our results are shown in Fig. 13. In Fig. 6, we confirm that ML2/$\alpha_{\rm F_{max}}$ calibration does indeed better reproduce the overall shape of DB (and DBA, although not shown) convection zones.

Overall, the ML2/$\alpha_{\rm F_{max}}$ results are similar to ML2/$\alpha_{\rm S}$ and ML2/$\alpha_{\rm f}$ calibration. We find inefficient convection resulting in small convection zones. Montgomery & Kupka (2004) performed an equivalent calibration of maximum convective flux using their 1D non-local envelope models of DB white dwarfs. They found ML2/$\alpha \approx 0.5$ for $\log g$ = 8.0, 28 000 K $\leqslant T_{\rm eff} \leqslant$ 33 000 K DB models, whereas we find $0.64 \gtrsim$ ML2/$\alpha \gtrsim 0.5$ for the same atmospheric parameter range. Both studies therefore suggest that convection is less efficient than what is currently assumed. When comparing DA and DB white dwarfs in the regime of very inefficient convection (closed bottom models in our case), Montgomery & Kupka (2004) found that for given $F_{\rm convective}/F_{\rm total}$, DB stars have lower values of ML2/$\alpha_{\rm F_{max}}$, but larger convection zone sizes. They attribute this to the He II convection zone being deeper than the H I counterpart, allowing the same amount of convective flux to be transported more efficiently and therefore with a

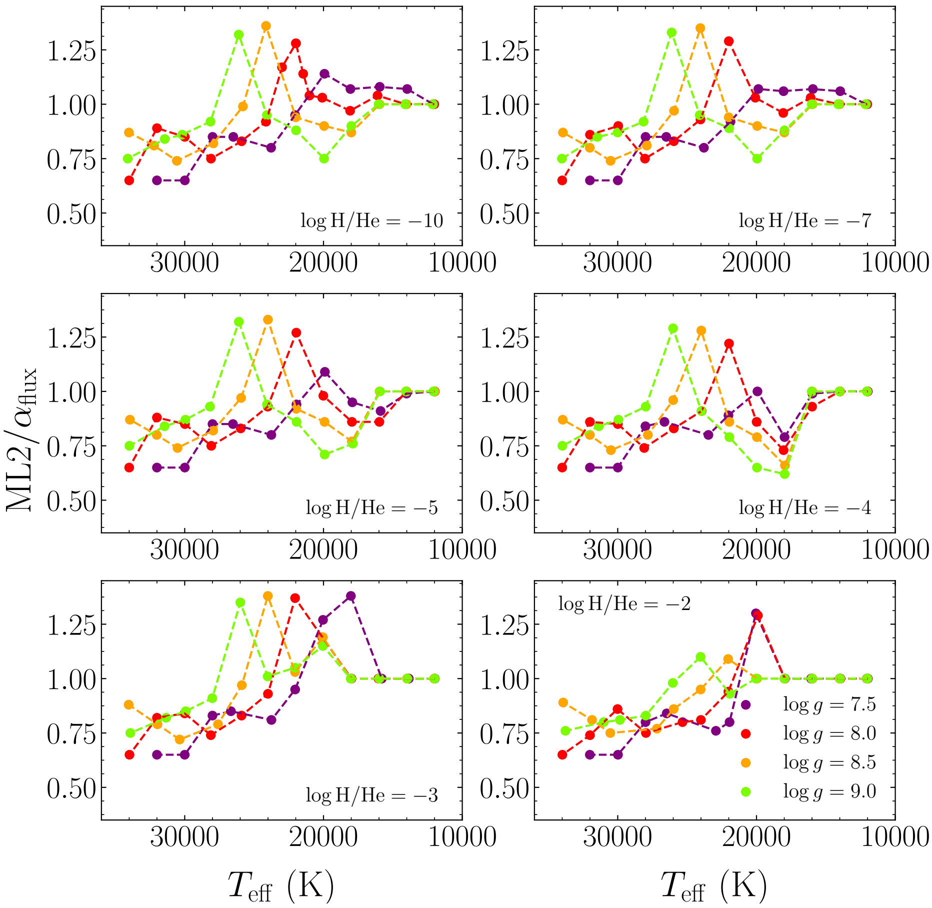

Figure 11. Same as Fig. 10 but for the flux boundary.

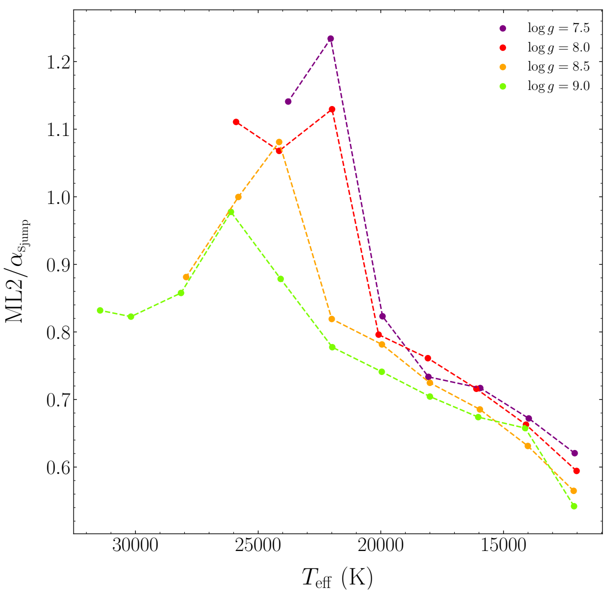

Figure 12. The calibrated mixing length parameter based on the entropy jump for open bottom 3D DB models. The solid colour points represent the ML2/$\alpha_{s_{\rm jump}}$ values and are connected based on their $\log g$ for clarity.

smaller value of ML2/α. Comparing our results to the 3D DA calibration of Tremblay et al. (2015), we also find that DB white dwarfs have smaller ML2/$\alpha_{\rm F_{max}}$ values and larger convection zone sizes, in agreement with Montgomery & Kupka (2004) results.

5.3 Calibration of velocities

Unlike in 1D models, in 3D simulations we expect there to be significant macroscopic diffusion at the bottom of the convection zone caused by momenta of downflows. We refer to this region as the velocity overshoot region, which overlaps with the flux overshoot region shown in Fig. 6 where negative flux is found. The velocity overshoot both includes and extends beyond the flux overshoot region. The overshoot region can be thought of as an extension to the more traditional convection zones discussed in this paper, especially for studies of metal diffusion in the atmospheres of white dwarfs. If included, it would mean larger convection zones than presented in this paper. In Fig. 14 we compare the velocities of our ⟨3D⟩ and 1D structures. In 1D the convective velocities are only non-zero inside the Schwarzschild convection zone, whereas in 3D, the velocities are significant even beyond the Schwarzschild and flux boundaries. As long as these convective velocities result in a macroscopic diffusion process that

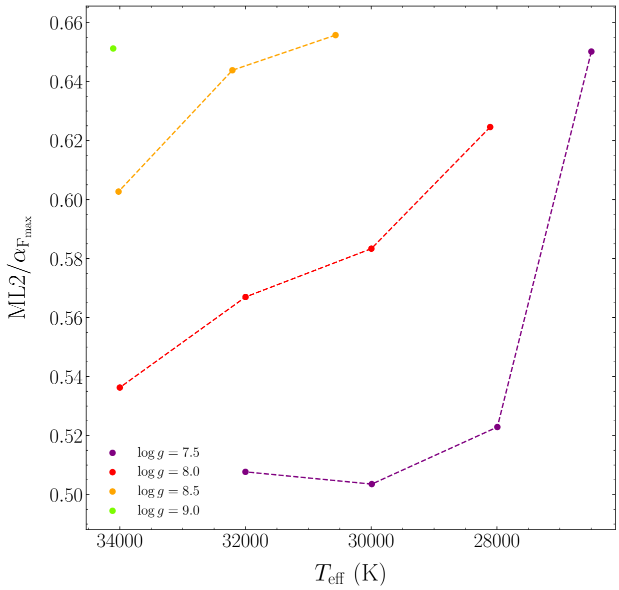

Figure 13. Same as Fig. 12, but for ML2/α calibration based on the maximum convective flux for 3D closed bottom models.

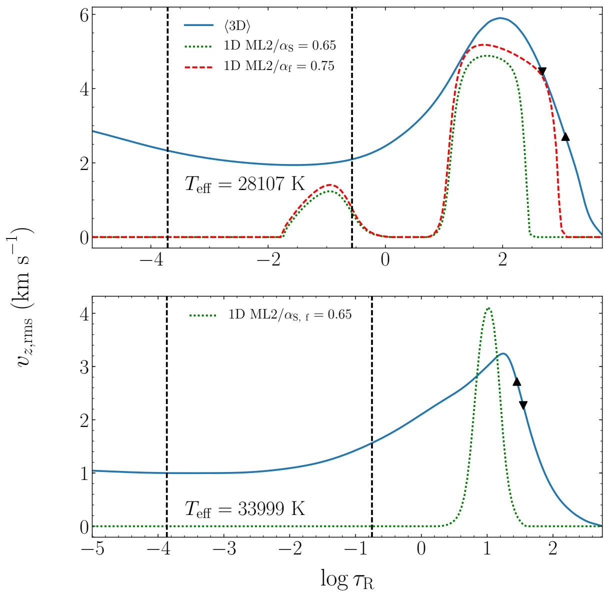

Figure 14. The vertical root mean square velocity as a function of $\log \tau_{\rm R}$ at two different $T_{\rm eff}$ for $\log g$ = 8.0 DB models. The ⟨3D⟩ $v_{z,\rm rms}$ is shown in solid blue. The 1D models with ML2/α = ML2/$\alpha_{\rm S}$ and ML2/$\alpha_{\rm f}$ are shown as dotted green and red dashed lines, respectively. The bottom of the Schwarzschild and flux boundaries are shown as downward- and upward-pointing triangles. The dashed black lines indicate the top and bottom of the optical light forming region. The 1D structures are unable to reproduce ⟨3D⟩ velocities especially outside the convective regions. In the upper layers ($\log \tau_{\rm R} <$ -3), the ⟨3D⟩ convective velocities have an important contribution from waves in the simulation.

is more efficient than microscopic diffusion, metals are expected to be fully mixed in the convection zone rather than diffuse out of it. Convective overshoot could also significantly enhance the dredge-up of carbon from the interior (Dufour et al. 2005) if the size of the superficial helium layer is small enough to allow convection to reach the underlying carbon layer.

Macroscopic diffusion can only be studied in 3D models with closed bottom. Yet, it is expected that all 3D models, including those with open bottom, will have overshoot both at the bottom and top of their convection zones, due to the dynamics of the convective flows. In order to study velocity overshoot for lower $T_{\rm eff}$ at which we currently only have open bottom models, a new grid of deep closed bottom models would have to be calculated.

Cunningham et al. (2019) have recently performed an in-depth study of overshoot in 3D DA closed models, finding that the mixed masses can be as much as 3 dex larger than currently used. Such a study for 3D DB and DBA models is beyond the scope of the current paper. As such, we do not attempt to perform any ML2/α calibration based on velocities.

5.4 Impact of metals on size of the convection zone

In order to test the effect of metals on the size of the convection zone, we calculate two sets of 3D models with and without metals at two selected $T_{\rm eff}$ values. We use the 1D atmospheric code of Koester (2010) to calculate input equations of state and opacity tables. When including metals, we use the metal composition and abundances of SDSS J073842.56+183509.06 determined by Dufour et al. (2012), as well as their determined hydrogen abundance of $\log({\rm H/He}) = -5.73 \pm 0.17$. We base our atmospheric composition on this white dwarf because it is one of the most polluted objects with 14 elements heavier than helium present in its atmosphere. Our aim is not to replicate exactly the atmospheric parameters determined by Dufour et al. (2012) but rather to study the effect of strong metal pollution on 3D models.

We start our models from two computed simulations of the 3D DBA grid with $\log({\rm H/He}) = -5.0$, $\log g = 8.0$ and $T_{\rm eff} \approx 14\,000$ K and $\approx 20\,000$ K. As $\log({\rm H/He})$ is ultimately controlled by the input tables, the $\log({\rm H/He})$ value of the starting model does not matter, but for convergence it is desirable to start with the closest available hydrogen abundance. Although, a value of $\log g = 8.4 \pm 0.2$ was determined by Dufour et al. (2012), we instead use $\log g = 8.0$, more in line with the recent determination of $\log g = 8.05 \pm 0.15$ by Gentile Fusillo et al. (2019a,b).

As $T_{\rm eff}$ is only recovered after the model is run, for each set of models we tried to achieve an agreement of around 100 K between the models with and without metals. We find that including our selected metal-rich composition in a 3D model decreases the $T_{\rm eff}$ by around 1 500 K given the specified inflowing entropy at the bottom boundary (using the same entropy zero point). For example, the non-metal $T_{\rm eff}$ value of one model is 13 975 K, whereas the $T_{\rm eff}$ of the metal version is 12 497 K with the same physical conditions at the bottom. In order to get an agreement of ≈ 100 K between models with and without metals, we had to increase the entropy of the inflowing material at the bottom boundary. From Figs. 2 and 3 it is clear that higher inflowing entropy means smaller convection zone. Therefore, we can speculate that with the inclusion of metals, the size of the convection zone becomes smaller for the same $T_{\rm eff}$. This is not unexpected, since similarly to hydrogen, metals increase the total opacity.

To find the mass of the convection zone we utilise the envelope code described in Koester & Kepler (2015) with our calibrated ML2/α parameter. The code takes the last point in a given ⟨3D⟩ atmospheric structure as a starting point for calculating the corresponding envelope. The envelope code is 1D and therefore depends on the mixing length theory. As per our calibration based on log (H/He) = −5.0, log g = 8.0 3D models, we use ML2/α = 1.0 and 0.80 for $T_{\rm eff} \approx$ 14 000 K and 20 000 K models, respectively. We do not perform any additional mixing length parameter calibration beyond what has been described in previous sections. The total mass of the white dwarf is assumed to be $0.59 M_\odot$ with radius of $0.0127 R_\odot$. The Saumon et al. (1995) equation of state is used and only hydrogen and helium atoms are considered. Metals are ignored as they do not impact the envelope structure as long as they are a trace species. Therefore, the difference in the mass of the convection zone between the metal and non-metal models arises from the fact that the 3D atmospheric structures are different (see Fig. 15). In Tab. 1 we show the change in the mass of the convection zone with the addition of metals. We find that in the $T_{\rm eff} \approx$ 14 000 K case, the mass of the convection zone decreases by a factor of 2 (or 0.31 dex) when metals are included. For the $T_{\rm eff} \approx$ 20 000 K case, a similar change of 0.45 dex is observed. In both cases it would mean that for the same metal abundance observed, the total mass of metals present would be smaller using the appropriate metal-rich model atmosphere. For $T_{\rm eff} \approx$ 14 000 K, the change in the mass of the convection zone with the inclusion of metals can be mimicked by increasing the hydrogen abundance from log (H/He) = −5.0 to −3.0. Similarly, at $T_{\rm eff} \approx$ 20 000 K, the increase of log (H/He) from −5.0 to somewhere between −3.0 and −2.0 gives a change in mass similar to the effect of metals.

In terms of the 3D picture, the effect of metals on the size of the convection zone is moderate, especially since SDSS J073842.56+183509.06 is one of the most heavily polluted white dwarfs. However, the effect of metals on spectroscopic 3D corrections for $T_{\rm eff}$ and log g are still to be explored. Fig. 15 suggests that changes in the structure of the light forming layers are important especially at lower Teff.

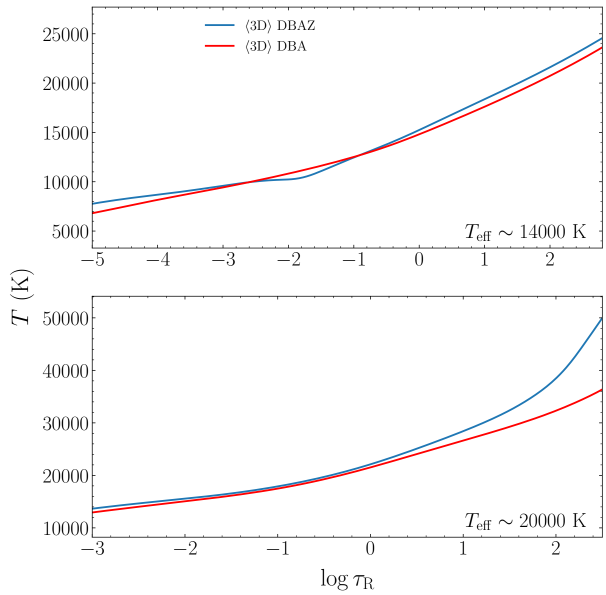

Figure 15. Temperature stratification of 3D models with and without metals at two different $T_{\rm eff}$ values. The ⟨3D⟩ structures for 3D DBAZ models are shown in solid blue, whereas the non-metal 3D models are in plotted in solid red.

Table 1. Change in the convection zone mass from addition of metals (DBAZ) in a helium-rich DBA white dwarf. The DBAZ models use the metal abundances of SDSS J073842.56+183509.06 determined by Dufour et al. (2012).

log g	$T_{\rm eff}$ (K)	Change in convection zone mass (dex)
8.0	≈ 14 000 K	−0.31
8.0	≈ 20 000 K	−0.45

6 SUMMARY

With 285 3D CO^{5}BOLD atmospheric models of DB and DBA white dwarfs, we have calibrated the mixing length parameter for the use of 1D envelope and evolutionary models. Our results are applicable for studies in need of convection zone sizes, for example for asteroseismological and remnant planetary systems analyses.

As the nature of the convection zone boundaries is more complex in 3D than in 1D, two definitions of the boundary were used for calibration, the Schwarzschild and flux boundaries. Overall, values of both ML2/$\alpha_{\rm S}$ or ML2/$\alpha_{\rm f}$ are lower than what is typically used in envelope and evolutionary models, meaning that convection is less efficient in 3D models. On average, for log g = 8.0 models with 18 000 K $\lesssim T_{\rm eff} \lesssim$ 30 000 K, we find ML2/$\alpha_{\rm S} \approx$ 0.80 and ML2/$\alpha_{\rm f} \approx$ 0.9. This is similar to ML2/α parameters calibrated for 3D DA white dwarfs (Tremblay et al. 2015).

Near the blue edge of the DBV instability strip, we find that the calibrated ML2/α values are much lower than the value of 1.25 recently used in the theoretical seismological study of Van Grootel et al. (2017). Therefore, in 3D, efficient convective energy transport sets in at a lower $T_{\rm eff}$. As the set-in of significant energy transport by convection is related to the blue edge of the strip, the 3D results would potentially mean lower $T_{\rm eff}$ of the theoretical blue edge. Note that compared to the empirical blue edge of $T_{\rm eff} \approx 31\,000$ K at $\log g \approx 7.8$ (Shipman et al. 2002; Provencal et al. 2003; Hermes et al. 2017; Cukanovaite et al. 2018), the current 1D theoretical blue edge of $T_{\rm eff} \approx 29\,000$ K at $\log g \approx 7.8$ is already too low in comparison (see Fig. 4 of Van Grootel et al. 2017).

In terms of determining the $T_{\rm eff}$ and $\log g$ values from spectroscopy, we recommend using ML2/α = 1.25 (but see Cukanovaite et al. 2018 for details of 3D DB corrections). However, it is clear that the actual efficiency of convection in the atmosphere has little to do with the ML2/α = 1.25 value calibrated from spectroscopic observations.

The current evolutionary models of white dwarfs can be improved by including our ML2/α calibrated values. 3D models also provide the best available estimate for the masses of convection zones of DB and DBA white dwarfs which are relevant for studies of remnant planetary systems. We illustrate this by calculating example 3D DBAZ models. However, our calibration does not consider velocity overshoot which could increase the mixing mass by orders of magnitude. In most of the models presented here, however, we cannot currently do any overshoot studies as the convection zones are too large to model. For the select few models at the highest $T_{\rm eff}$ of our grid, the overshoot region can be directly accessed and could be used for direct investigation, similar to what has been achieved for DA white dwarfs (Cunningham et al. 2019).

Convection is not expected to have any direct impact of the derived ages of white dwarfs, up until the convection zone grows large enough to reach the core, directly coupling the degenerate core to the surface (Tremblay et al. 2015). This occurs at $T_{\rm eff} \sim 5\,000$ K for DA white dwarfs (Tassoul et al. 1990; Tremblay et al. 2015) and $\sim 10\,000$ K for DB white dwarfs (Tassoul et al. 1990; MacDonald & Vennes 1991). However, at these $T_{\rm eff}$ convection is adiabatic and therefore loses its sensitivity to the ML2/α parameter. Therefore, we do not expect our calibration of the ML2/α parameter to have any direct impact on the ages derived from evolutionary models. However, the 3D models can have an indirect effect on age determinations due to 3D spectroscopic corrections for $\log g$ and $T_{\rm eff}$ (Cukanovaite et al. 2018). 3D DBA spectroscopic corrections will be derived in a future work.

ACKNOWLEDGEMENTS

We would like to thank the anonymous referee for their helpful comments. This project has received funding from the European Research Council (ERC) under the European Union's Horizon 2020 research and innovation programme (grant agreement No 677706 - WD3D). B.F. has been supported by the Swedish Research Council (Vetenskapsrådet). H.G.L. acknowledges financial support by the Sonderforschungsbereich SFB 881 "The Milky Way System" (subprojects A4) of the German Research Foundation (DFG).

REFERENCES

Althaus L. G., Benvenuto O. G., 1996, MNRAS, 278, 981
Althaus L. G., Benvenuto O. G., 1997, MNRAS, 288, L35
Althaus L. G., Córsico A. H., Isern J., García-Berro E., 2010, A&ARv, 18, 471
Beauchamp A., Wesemael F., Bergeron P., 1997, ApJS, 108, 559
Benvenuto O. G., Althaus L. G., 1999, MNRAS, 303, 30
Bergeron P., Wesemael F., Fontaine G., 1992, ApJ, 387, 288
Bergeron P., Wesemael F., Lamontagne R., Fontaine G., Saffer R. A., Allard N. F., 1995, ApJ, 449, 258
Bergeron P., et al., 2011, ApJ, 737, 28
Böhm-Vitense E., 1958, Z. Astrophys., 46, 108
Canuto V. M., 2007, in Kupka F., Roxburgh I., Chan K. L., eds, IAU Symposium Vol. 239, Convection in Astrophysics. pp 3–18, doi:10.1017/S1743921307000051
Canuto V. M., Mazzitelli I., 1991, ApJ, 370, 295
Canuto V. M., Mazzitelli I., 1992, ApJ, 389, 724
Canuto V. M., Goldman I., Mazzitelli I., 1996, ApJ, 473, 550
Cattaneo F., Brummell N. H., Toomre J., Malagoli A., Hurlburt N. E., 1991, ApJ, 370, 282
Córsico A. H., Althaus L. G., 2016, A&A, 585, A1
Córsico A. H., Althaus L. G., Miller Bertolami M. M., García-Berro E., 2009, in Journal of Physics Conference Series. p. 012075 (`arXiv:0810.2963`), doi:10.1088/1742-6596/172/1/012075
Cukanovaite E., Tremblay P.-E., Freytag B., Ludwig H.-G., Bergeron P., 2018, MNRAS, 481, 1522
Cunningham T., Tremblay P.-E., Freytag B., Ludwig H.-G., Koester D., 2019, Monthly Notices of the Royal Astronomical Society, 488, 2503
Dufour P., Bergeron P., Fontaine G., 2005, ApJ, 627, 404
Dufour P., Kilic M., Fontaine G., Bergeron P., Melis C., Bochanski J., 2012, ApJ, 749, 6
Fontaine G., Brassard P., 2008, PASP, 120, 1043
Fontaine G., van Horn H. M., 1976, ApJS, 31, 467
Fontaine G., Tassoul M., Wesemael F., 1984, in Liege International Astrophysical Colloquia. pp 328–332
Fontaine G., Brassard P., Bergeron P., 2001, PASP, 113, 409
Freytag B., 2013, Memorie della Societa Astronomica Italiana Supplementi, 24, 26
Freytag B., 2017, Mem. Soc. Astron. Italiana, 88, 12
Freytag B., Ludwig H.-G., Steffen M., 1996, A&A, 313, 497
Freytag B., Steffen M., Dorch B., 2002, Astronomische Nachrichten, 323, 213
Freytag B., Steffen M., Ludwig H.-G., Wedemeyer-Böhm S., Schaffenberger W., Steiner O., 2012, Journal of Computational Physics, 231, 919
Gaia Collaboration et al., 2018, A&A, 616, A1
Genest-Beaulieu C., Bergeron P., 2019, arXiv e-prints,
Gentile Fusillo N. P., Gänsicke B. T., Farihi J., Koester D., Schreiber M. R., Pala A. F., 2017, MNRAS, 468, 971
Gentile Fusillo N. P., et al., 2019a, MNRAS, 482, 4570
Gentile Fusillo N. P., et al., 2019b, VizieR Online Data Catalog, 748
Hermes J. J., Kawaler S. D., Bischoff-Kim A., Provencal J. L., Dunlap B. H., Clemens J. C., 2017, ApJ, 835, 277
John T. L., 1994, MNRAS, 269, 871
Kepler S. O., et al., 2015, MNRAS, 446, 4078
Kleinman S. J., et al., 2013, ApJS, 204, 5
Koester D., 2009, A&A, 498, 517
Koester D., 2010, Mem. Soc. Astron. Italiana, 81, 921
Koester D., Kepler S. O., 2015, A&A, 583, A86
Koester D., Allard N. F., Vauclair G., 1994, A&A, 291, L9
Kupka F., Zaussinger F., Montgomery M. H., 2018, MNRAS, 474, 4660
Ludwig H.-G., Jordan S., Steffen M., 1993, in Barstow M. A., ed., NATO Advanced Science Institutes (ASI) Series C Vol. 403, NATO Advanced Science Institutes (ASI) Series C. p. 471
Ludwig H.-G., Jordan S., Steffen M., 1994, A&A, 284, 105
Ludwig H.-G., Freytag B., Steffen M., 1999, A&A, 346, 111
MacDonald J., Vennes S., 1991, ApJ, 371, 719
Magic Z., Collet R., Asplund M., Trampedach R., Hayek W., Chiavassa A., Stein R. F., Nordlund Å., 2013, A&A, 557, A26
Magic Z., Weiss A., Asplund M., 2015, A&A, 573, A89
Montgomery M. H., Kupka F., 2004, MNRAS, 350, 267
Mosumgaard J. R., Ball W. H., Silva Aguirre V., Weiss A., Christensen-Dalsgaard J., 2018, MNRAS, 478, 5650
Nordlund A., 1982, A&A, 107, 1
Provencal J. L., Shipman H. L., Riddle R. L., Vuckovic M., 2003, in de Martino D., Silvotti R., Solheim J.-E., Kalytis R., eds, NATO ASIB Proc. 105: White Dwarfs Vol. 105, NATO ASIB Proc. 105: White Dwarfs. p. 235
Rolland B., Bergeron P., Fontaine G., 2018, ApJ, 857, 56
Salaris M., Cassisi S., 2015, A&A, 577, A60
Saumon D., Chabrier G., van Horn H. M., 1995, ApJS, 99, 713
Schatzman E., 1948, Nature, 161, 61
Shipman H. L., 1979, ApJ, 228, 240
Shipman H. L., Provencal J., Riddle R., Vuckovic M., 2002, in American Astronomical Society Meeting Abstracts #200. p. 765
Sonoi T., Ludwig H.-G., Dupret M.-A., Montalbán J., Samadi R., Belkacem K., Caffau E., Goupil M.-J., 2019, A&A, 621, A84
Steffen M., 1993, in Weiss W. W., Baglin A., eds, Astronomical Society of the Pacific Conference Series Vol. 40, IAU Colloq. 137: Inside the Stars. p. 300
Stein R. F., Nordlund A., 1989, ApJ, 342, L95
Tassoul M., Fontaine G., Winget D. E., 1990, ApJS, 72, 335
Thejll P., Vennes S., Shipman H. L., 1991, ApJ, 370, 355
Trampedach R., Stein R. F., Christensen-Dalsgaard J., Nordlund Å., Asplund M., 2014, MNRAS, 445, 4366
Tremblay P.-E., Bergeron P., 2009, ApJ, 696, 1755
Tremblay P.-E., Ludwig H.-G., Steffen M., Freytag B., 2013a, A&A, 552, A13
Tremblay P.-E., Ludwig H.-G., Freytag B., Steffen M., Caffau E., 2013b, A&A, 557, A7
Tremblay P.-E., Ludwig H.-G., Steffen M., Freytag B., 2013c, A&A, 559, A104
Tremblay P.-E., Ludwig H.-G., Freytag B., Fontaine G., Steffen M., Brassard P., 2015, ApJ, 799, 142
Tremblay P.-E., Cukanovaite E., Gentile Fusillo N. P., Cunningham T., Hollands M. A., 2019, MNRAS, 482, 5222
Van Grootel V., Fontaine G., Brassard P., Dupret M.-A., 2017, in Tremblay P.-E., Gaensicke B., Marsh T., eds, Astronomical Society of the Pacific Conference Series Vol. 509, 20th European White Dwarf Workshop. p. 321
Veras D., 2016, Royal Society Open Science, 3, 150571
Vögler A., Bruls J. H. M. J., Schüssler M., 2004, A&A, 421, 741
Wedemeyer S., Freytag B., Steffen M., Ludwig H.-G., Holweger H., 2004, A&A, 414, 1121
Wesemael F., Beauchamp A., Bergeron P., Fontaine G., Brassard P., Saffer R. A., Liebert J., 1999, in Gimenez A., Guinan E. F., Montesinos B., eds, Astronomical Society of the Pacific Conference Series Vol. 173, Stellar Structure: Theory and Test of Connective Energy Transport. p. 325
Winget D. E., van Horn H. M., Tassoul M., Fontaine G., Hansen C. J., Carroll B. W., 1982, ApJ, 252, L65
Winget D. E., van Horn H. M., Tassoul M., Hansen C. J., Fontaine G., 1983, ApJ, 268, L33
Zahn J.-P., 1991, A&A, 252, 179

This paper has been typeset from a TEX/LATEX file prepared by the author.

APPENDIX A: ADDITIONAL INFORMATION

Tabs. A1 to A6 list some basic parameters of the 3D simulations. This includes the surface gravity of a given simulation, its effective temperature, the size of the box the simulation was run in, the run time and the relative bolometric intensity contrast averaged over space and time.

Tabs. A7 to A12 list the parameters needed for the mixing length calibration of 3D open bottom models, as well as the results of the calibration. For each 3D simulation, its surface gravity, effective temperature and the adiabatic entropy used for ML2/α_S calibration is included. Also given are the ML2/α_S, $\log(M_{CVZ}/M_{tot})$, T and P values for the Schwarzschild boundary. $\log(M_{CVZ}/M_{tot})$, temperature and pressure are found from the 1D envelope calculated at ML2/α_S. The same parameters are also given for the flux boundary. As the flux boundary cannot be directly accessed for open bottom models, we instead use the relation ML2/α_f = 1.17 ML2/α_S to find ML2/α_f.

Tabs. A13 to A18 list the parameters needed for the calibration of the mixing length for 3D closed bottom models, as well as the results of the calibration. For each 3D simulation, its surface gravity and effective temperature are given. The mixing length calibration for closed bottom model relies on the spatially- and temporally-averaged 3D temperature and pressure at the bottom of the convection zone, and these parameters are given for both the Schwarzschild and flux boundaries. The ML2/α_S and ML2/α_f are also given, as well as the $\log(M_{CVZ}/M_{tot})$ for each boundary.

Table A1. Select parameters of the 3D DB model atmospheres, where $\delta I_{rms}/\langle I\rangle$ is the relative bolometric intensity contrast averaged over space and time.

$\log g$	T_{eff} (K)	Box size (km × km × km)	Total run time (stellar s)	$\delta I_{rms}/\langle I\rangle$ (%)
7.5	12098	1.22×1.22×0.58	33.6	3.6
7.5	13969	1.98×1.98×0.67	32.2	8.9
7.5	15947	2.86×2.86×1.19	32.2	16.4
7.5	18059	6.09×6.09×1.46	32.1	21.3
7.5	19931	11.96×11.96×2.39	34.7	23.4
7.5	22044	21.75×21.75×4.51	32.3	25.5
7.5	23774	23.96×23.96×4.78	31.7	24.3
7.5	26497	37.47×37.47×21.40	32.6	21.7
7.5	27993	31.22×31.22×10.77	14.7	17.5
7.5	29991	31.22×31.22×11.86	17.7	9.4
7.5	32001	33.48×33.48×14.00	48.3	4.8
8.0	12020	0.70×0.70×0.10	10.0	2.1
8.0	14083	0.79×0.79×0.24	10.2	6.0
8.0	16105	0.94×0.94×0.18	10.1	11.9
8.0	18082	1.23×1.23×0.35	13.0	17.0
8.0	20090	2.00×2.00×0.58	12.5	19.4
8.0	21014	5.19×5.19×0.97	11.9	21.0
8.0	21465	5.19×5.19×0.97	11.0	21.6
8.0	21987	5.19×5.19×0.97	8.7	22.3
8.0	22988	8.62×8.62×1.41	11.6	24.2
8.0	24144	8.62×8.62×1.41	11.7	23.8
8.0	25898	8.62×8.62×1.56	10.0	21.1
8.0	28107	12.63×12.63×4.93	16.8	20.3
8.0	29997	12.63×12.63×5.12	13.5	19.2
8.0	31999	12.63×12.63×3.28	5.0	14.8
8.0	33999	12.63×12.63×3.42	5.3	7.9
8.5	12139	0.25×0.25×0.05	3.6	1.5
8.5	14007	0.25×0.25×0.04	5.7	3.6
8.5	15961	0.34×0.34×0.05	3.5	7.6
8.5	18000	0.39×0.39×0.13	3.6	12.6
8.5	19955	0.60×0.60×0.20	4.0	15.5
8.5	21999	1.03×1.03×0.26	3.2	17.8
8.5	24143	1.78×1.78×0.37	3.7	22.1
8.5	25805	2.37×2.37×0.44	3.5	22.3
8.5	27934	2.53×2.53×0.59	2.9	20.6
8.5	30567	4.53×4.53×1.97	4.6	19.5
8.5	32208	4.53×4.53×2.12	3.8	18.9
8.5	34020	4.53×4.53×1.92	3.7	17.6
9.0	12124	0.06×0.06×0.01	3.4	0.8
9.0	14117	0.07×0.07×0.01	2.0	2.3
9.0	16029	0.11×0.11×0.02	1.1	5.0
9.0	17998	0.12×0.12×0.03	1.1	8.7
9.0	19961	0.14×0.14×0.05	1.0	11.7
9.0	21978	0.20×0.20×0.07	1.0	13.6
9.0	24082	0.39×0.39×0.10	1.1	17.2
9.0	26109	0.76×0.76×0.13	0.6	20.6
9.0	28143	0.76×0.76×0.16	1.0	20.6
9.0	30184	0.86×0.86×0.20	1.1	17.4
9.0	31440	0.86×0.86×0.20	3.2	17.2
9.0	34105	1.43×1.43×0.84	2.3	18.3

Table A2. Select parameters of 3D DBA model atmospheres with log H/He = −7.

log g	$T_{\rm eff}$ (K)	Box size (km × km × km)	Total run time (stellar s)	$\delta I_{\rm rms}/\langle I \rangle$ (%)
7.5	12098	1.22×1.22×0.58	32.8	3.6
7.5	13967	1.98×1.98×0.67	31.7	8.8
7.5	15936	2.86×2.86×1.19	35.0	16.3
7.5	18051	6.09×6.09×1.46	34.1	21.0
7.5	19865	11.96×11.96×2.44	32.6	22.3
7.5	21873	21.75×21.75×4.04	37.8	22.7
7.5	23789	23.96×23.96×4.80	32.1	24.4
7.5	26501	37.47×37.47×21.40	33.2	22.1
7.5	27993	31.22×31.22×10.77	16.0	17.2
7.5	29993	31.22×31.22×11.86	18.3	10.2
7.5	32002	33.48×33.48×14.00	34.4	4.5
8.0	12019	0.70×0.70×0.11	10.8	2.1
8.0	14083	0.79×0.79×0.24	10.9	5.9
8.0	16099	0.94×0.94×0.19	10.1	11.9
8.0	18074	1.23×1.23×0.35	10.3	17.0
8.0	20088	2.00×2.00×0.58	10.2	19.4
8.0	21996	5.19×5.19×0.97	11.4	22.3
8.0	24036	8.62×8.62×1.41	10.4	24.0
8.0	25956	8.62×8.62×1.56	10.2	21.1
8.0	28037	12.63×12.63×4.93	18.2	20.6
8.0	29963	12.63×12.63×5.12	10.5	20.2
8.0	32000	12.63×12.63×3.28	5.5	14.4
8.0	33999	12.63×12.63×3.42	5.4	8.5
8.5	12147	0.25×0.25×0.05	3.1	1.5
8.5	14004	0.25×0.25×0.04	3.8	3.6
8.5	15958	0.34×0.34×0.05	3.3	7.6
8.5	17998	0.39×0.39×0.13	3.6	12.6
8.5	19951	0.60×0.60×0.20	3.4	15.5
8.5	22002	1.03×1.03×0.26	3.1	17.9
8.5	24047	1.78×1.78×0.37	3.3	22.1
8.5	25943	2.37×2.37×0.44	3.4	22.1
8.5	27907	2.53×2.53×0.59	3.2	20.6
8.5	30514	4.53×4.53×1.97	4.2	19.7
8.5	32012	4.53×4.53×2.12	3.7	19.0
8.5	33949	4.53×4.53×1.92	3.2	17.1
9.0	12120	0.06×0.06×0.01	1.1	0.8
9.0	14114	0.07×0.07×0.01	1.0	2.3
9.0	16026	0.11×0.11×0.02	1.0	4.9
9.0	17985	0.12×0.12×0.03	1.0	8.7
9.0	19957	0.14×0.14×0.04	1.1	11.7
9.0	21982	0.20×0.20×0.07	1.1	13.6
9.0	24093	0.39×0.39×0.10	1.1	17.1
9.0	26115	0.76×0.76×0.13	1.1	20.7
9.0	28141	0.76×0.76×0.16	1.1	20.6
9.0	30006	0.86×0.86×0.20	1.0	17.8
9.0	31472	0.86×0.86×0.20	1.3	16.7
9.0	34021	1.43×1.43×0.84	2.0	18.3

Table A3. Select parameters of 3D DBA model atmospheres with log H/He = −5.

log g	$T_{\rm eff}$ (K)	Box size (km × km × km)	Total run time (stellar s)	$\delta I_{\rm rms}/\langle I \rangle$ (%)
7.5	12009	1.22×1.22×0.59	33.1	3.4
7.5	14013	1.98×1.98×0.67	33.0	9.0
7.5	15886	2.86×2.86×1.19	33.9	15.7
7.5	17920	6.09×6.09×1.46	31.8	21.0
7.5	19900	11.96×11.96×2.44	32.2	23.1
7.5	21946	21.75×21.75×4.51	32.6	24.7
7.5	23757	23.96×23.96×4.80	32.2	24.2
7.5	26522	37.47×37.47×21.40	36.4	22.1
7.5	27998	31.22×31.22×10.77	15.8	17.7
7.5	29992	31.22×31.22×11.86	26.6	9.7
7.5	32002	33.48×33.48×14.00	24.0	5.1
8.0	11978	0.70×0.70×0.11	10.2	2.1
8.0	14031	0.79×0.79×0.24	9.9	5.7
8.0	15974	0.94×0.94×0.19	11.5	11.3
8.0	17952	1.23×1.23×0.35	10.4	16.9
8.0	20012	2.00×2.00×0.58	12.7	19.4
8.0	21959	5.19×5.19×0.97	10.1	22.2
8.0	24014	8.62×8.62×1.41	10.0	24.0
8.0	25963	8.62×8.62×1.56	9.9	20.6
8.0	28086	12.63×12.63×4.93	12.4	20.7
8.0	29989	12.63×12.63×5.12	10.1	18.9
8.0	32002	12.63×12.63×3.28	10.3	14.7
8.0	34000	12.63×12.63×3.42	10.1	8.2
8.5	11996	0.25×0.25×0.05	4.0	1.3
8.5	14012	0.25×0.25×0.04	3.7	3.5
8.5	15957	0.34×0.34×0.05	3.7	7.6
8.5	17956	0.39×0.39×0.13	3.6	12.7
8.5	19924	0.60×0.60×0.20	4.0	15.5
8.5	21962	1.03×1.03×0.26	3.7	17.8
8.5	24004	1.78×1.78×0.37	3.7	21.9
8.5	25938	2.37×2.37×0.45	3.7	22.2
8.5	27946	2.53×2.53×0.59	3.5	20.3
8.5	30517	4.53×4.53×1.97	4.1	19.5
8.5	32015	4.53×4.53×2.12	4.3	19.0
8.5	33947	4.53×4.53×1.92	3.6	17.4
9.0	12077	0.06×0.06×0.01	1.1	0.8
9.0	14059	0.07×0.07×0.01	1.1	2.2
9.0	15930	0.11×0.11×0.02	1.0	4.7
9.0	17885	0.12×0.12×0.03	1.0	8.7
9.0	19922	0.14×0.14×0.04	1.1	11.8
9.0	21942	0.20×0.20×0.07	1.1	13.6
9.0	24076	0.39×0.39×0.10	1.1	17.1
9.0	26099	0.76×0.76×0.13	1.0	20.6
9.0	28181	0.76×0.76×0.16	1.0	20.6
9.0	29952	0.86×0.86×0.20	1.0	17.8
9.0	31452	0.86×0.86×0.20	1.0	17.2
9.0	33986	1.43×1.43×0.84	2.3	18.3

Table A4. Select parameters of 3D DBA model atmospheres with log H/He = −4.

log g	$T_{\rm eff}$ (K)	Box size (km × km × km)	Total run time (stellar s)	$\delta I_{\rm rms}/\langle I \rangle$ (%)
7.5	11983	1.22×1.22×0.58	32.0	3.5
7.5	13985	1.98×1.98×0.67	31.8	9.0
7.5	15973	2.86×2.86×1.19	34.0	16.0
7.5	17979	6.09×6.09×1.46	34.2	20.4
7.5	19932	11.96×11.96×2.75	34.5	22.2
7.5	22021	21.75×21.75×4.51	32.2	23.8
7.5	23464	23.96×23.96×4.80	31.0	23.7
7.5	26632	37.47×37.47×21.40	34.4	21.9
7.5	28004	31.22×31.22×10.77	15.8	17.3
7.5	29993	31.22×31.22×11.86	19.8	9.4
7.5	32002	33.48×33.48×14.00	10.9	5.3
8.0	12008	0.70×0.70×0.11	10.0	2.2
8.0	13999	0.79×0.79×0.24	10.1	5.8
8.0	15994	0.94×0.94×0.19	10.3	11.4
8.0	18052	1.23×1.23×0.35	10.1	17.1
8.0	19991	2.00×2.00×0.58	10.2	19.5
8.0	21981	5.19×5.19×1.02	10.0	22.0
8.0	23953	8.62×8.62×1.41	10.3	23.3
8.0	25961	8.62×8.62×1.56	10.2	20.6
8.0	28092	12.63×12.63×4.93	10.2	21.1
8.0	29994	12.63×12.63×5.12	11.9	19.4
8.0	32002	12.63×12.63×3.28	10.4	14.5
8.0	34000	12.63×12.63×3.42	10.1	8.0
8.5	12027	0.25×0.25×0.05	3.8	1.4
8.5	13981	0.25×0.25×0.04	3.7	3.6
8.5	15982	0.34×0.34×0.06	4.1	7.6
8.5	17951	0.39×0.39×0.13	3.8	13.0
8.5	19972	0.60×0.60×0.20	3.8	15.8
8.5	21956	1.03×1.03×0.26	3.8	18.0
8.5	23980	1.78×1.78×0.37	3.9	21.9
8.5	26006	2.37×2.37×0.46	3.6	21.5
8.5	27829	2.53×2.53×0.59	3.7	20.8
8.5	30490	4.53×4.53×1.97	3.8	19.4
8.5	32008	4.53×4.53×2.12	4.0	19.0
8.5	33963	4.53×4.53×1.92	3.3	17.4
9.0	12055	0.06×0.06×0.01	1.1	0.9
9.0	14023	0.07×0.07×0.01	1.0	2.2
9.0	16020	0.11×0.11×0.02	1.0	4.9
9.0	17972	0.12×0.12×0.03	1.1	9.3
9.0	19968	0.14×0.14×0.04	1.1	12.2
9.0	21957	0.20×0.20×0.07	1.0	13.9
9.0	23971	0.39×0.39×0.10	1.0	17.2
9.0	26018	0.76×0.76×0.13	1.0	20.5
9.0	27982	0.76×0.76×0.16	1.0	20.6
9.0	29948	0.86×0.86×0.20	1.0	17.8
9.0	31360	0.86×0.86×0.20	1.0	17.0
9.0	33988	1.43×1.43×0.84	1.7	18.3

Table A5. Select parameters of 3D DBA model atmospheres with log H/He = −3.

log g	$T_{\rm eff}$ (K)	Box size (km × km × km)	Total run time (stellar s)	$\delta I_{\rm rms}/\langle I \rangle$ (%)
7.5	11980	1.22×1.22×0.37	31.7	3.3
7.5	13855	1.98×1.98×0.67	36.3	8.8
7.5	15805	2.86×2.86×1.19	34.6	16.2
7.5	18026	6.09×6.09×1.46	32.1	21.2
7.5	20035	11.96×11.96×2.53	33.0	23.3
7.5	22043	21.75×21.75×4.51	31.6	24.8
7.5	23752	23.96×23.96×4.89	31.4	24.5
7.5	26670	37.47×37.47×21.40	35.7	21.0
7.5	28000	31.22×31.22×10.77	15.2	17.2
7.5	29999	31.22×31.22×11.86	22.8	8.8
7.5	32000	33.48×33.48×14.00	23.0	4.3
8.0	12007	0.70×0.70×0.12	11.9	2.1
8.0	13961	0.79×0.79×0.14	10.5	5.8
8.0	16040	0.94×0.94×0.19	10.1	11.6
8.0	17985	1.23×1.23×0.36	10.4	17.0
8.0	20088	2.00×2.00×0.58	10.1	19.5
8.0	22047	5.19×5.19×0.99	10.8	22.5
8.0	24002	8.62×8.62×1.41	10.4	24.0
8.0	25904	8.62×8.62×1.56	10.4	21.2
8.0	28118	12.63×12.63×4.93	11.4	21.4
8.0	30001	12.63×12.63×5.12	11.0	18.9
8.0	31999	12.63×12.63×3.28	10.0	14.1
8.0	33980	12.63×12.63×3.42	9.9	8.1
8.5	12027	0.25×0.25×0.05	3.8	1.3
8.5	13985	0.25×0.25×0.05	3.5	3.5
8.5	15988	0.34×0.34×0.06	3.4	7.6
8.5	18029	0.39×0.39×0.13	3.7	12.8
8.5	20043	0.60×0.60×0.20	3.6	15.7
8.5	22050	1.03×1.03×0.27	3.8	18.0
8.5	24011	1.78×1.78×0.37	3.4	22.0
8.5	25884	2.37×2.37×0.46	3.6	22.1
8.5	27602	2.53×2.53×0.59	3.1	21.5
8.5	30364	4.53×4.53×1.97	3.2	19.2
8.5	31965	4.53×4.53×2.12	5.2	18.8
8.5	34038	4.53×4.53×1.92	3.6	17.3
9.0	11994	0.06×0.06×0.01	1.0	0.8
9.0	13967	0.07×0.07×0.01	1.1	2.1
9.0	15970	0.11×0.11×0.02	1.1	4.8
9.0	18038	0.12×0.12×0.03	1.2	9.0
9.0	20045	0.14×0.14×0.04	1.0	12.0
9.0	22057	0.20×0.20×0.07	1.0	13.8
9.0	24026	0.39×0.39×0.10	1.0	17.1
9.0	25997	0.76×0.76×0.13	1.0	20.6
9.0	28015	0.76×0.76×0.16	1.0	20.6
9.0	29929	0.86×0.86×0.20	1.0	18.3
9.0	31340	0.86×0.86×0.20	1.0	17.5
9.0	33917	1.43×1.43×0.84	1.0	18.6

Table A6. Select parameters of 3D DBA model atmospheres with log H/He = −2.

$\log g$	$T_{\rm eff}$ (K)	Box size (km × km × km)	Total run time (stellar s)	$\delta I_{\rm rms}/\langle I \rangle$ (%)
7.5	11977	1.98×1.98×0.67	39.8	9.0
7.5	13995	2.86×2.86×1.19	38.3	15.0
7.5	16063	6.09×6.09×1.46	40.0	17.7
7.5	17963	6.09×6.09×1.46	73.4	20.2
7.5	20042	21.75×21.75×3.39	36.8	20.6
7.5	21944	21.75×21.75×4.59	33.9	18.2
7.5	22925	23.96×23.96×5.01	32.8	21.8
7.5	26471	37.47×37.47×21.40	33.7	19.7
7.5	27996	31.22×31.22×11.11	16.6	16.1
7.5	29982	31.22×31.22×11.86	24.1	8.0
7.5	32009	33.48×33.48×14.00	24.0	4.0
8.0	12044	0.79×0.79×0.16	14.0	5.8
8.0	13953	0.94×0.94×0.20	12.8	10.6
8.0	15983	1.23×1.23×0.36	14.4	14.3
8.0	17961	1.23×1.23×0.38	19.9	17.1
8.0	19903	3.40×3.40×0.69	23.1	18.4
8.0	22026	8.62×8.62×1.43	11.0	17.6
8.0	24006	8.62×8.62×1.53	11.9	19.3
8.0	25333	8.62×8.62×1.67	12.4	18.1
8.0	27968	12.63×12.63×4.93	11.5	20.2
8.0	30013	12.63×12.63×5.12	10.4	18.3
8.0	31997	12.63×12.63×3.39	10.2	12.5
8.0	33989	12.63×12.63×3.51	10.0	7.0
8.5	12013	0.25×0.25×0.05	5.1	3.4
8.5	14013	0.34×0.34×0.06	4.4	7.1
8.5	15994	0.39×0.39×0.13	6.1	10.6
8.5	17996	0.60×0.60×0.20	4.4	13.7
8.5	19962	0.60×0.60×0.20	7.1	15.1
8.5	22044	1.78×1.78×0.38	3.6	15.8
8.5	24025	2.37×2.37×0.46	3.5	19.7
8.5	25969	2.53×2.53×0.59	3.8	16.1
8.5	27179	3.80×3.80×0.62	4.6	17.4
8.5	30535	4.53×4.53×2.05	7.9	18.4
8.5	31852	4.53×4.53×2.12	3.5	18.7
8.5	33930	4.53×4.53×1.92	3.4	16.9
9.0	12025	0.07×0.07×0.01	1.2	2.0
9.0	13986	0.11×0.11×0.02	1.3	4.4
9.0	16001	0.12×0.12×0.03	1.6	7.3
9.0	17981	0.14×0.14×0.04	1.4	10.2
9.0	20038	0.14×0.14×0.05	2.0	12.0
9.0	21923	0.41×0.41×0.08	2.9	12.9
9.0	24031	0.76×0.76×0.13	1.0	17.7
9.0	26031	0.76×0.76×0.16	2.0	16.9
9.0	27980	0.86×0.86×0.20	1.1	16.3
9.0	29843	0.86×0.86×0.21	1.3	16.0
9.0	31011	0.86×0.86×0.22	2.3	16.7
9.0	33770	1.43×1.43×0.84	3.2	18.2

Table A7. MLT calibration for open bottom 3D DB models, where 3D $s_{\rm env}$ is the 3D adiabatic entropy used for calibration, ML2/$\alpha_{\rm S}$ is the calibrated ML2/α value for Schwarzschild boundary, $\log{(M_{\rm CVZ}/M_{\rm tot})_{\rm S}}$ is $\log{(M_{\rm CVZ}/M_{\rm tot})}$ for Schwarzschild boundary, $(\log{T_{\rm b}})_{\rm S}$ is the 1D calibrated temperature at the Schwarzschild boundary, $(\log{P_{\rm b}})_{\rm S}$ is the 1D calibrated pressure at the Schwarzschild boundary. The same parameters are also given for the flux boundary and are denoted by subscript 'f'.

$\log g$	$T_{\rm eff}$ (K)	3D $s_{\rm env}$ (10^9 erg g^{-1} K^{-1})	ML2/$\alpha_{\rm S}$	$\log{(M_{\rm CVZ}/M_{\rm tot})_{\rm S}}$	$(\log{T_{\rm b}})_{\rm S}$ (K)	$(\log{P_{\rm b}})_{\rm S}$ (dyn cm^{-2})	ML2/$\alpha_{\rm f}$	$\log{(M_{\rm CVZ}/M_{\rm tot})_{\rm f}}$	$(\log{T_{\rm b}})_{\rm f}$ (K)	$(\log{P_{\rm b}})_{\rm f}$ (dyn cm^{-2})
7.5	12098	0.40	1.00	−4.14	6.68	16.96	1.00	−4.14	6.68	16.96
7.5	13969	0.44	0.91	−4.56	6.63	16.53	1.07	−4.54	6.63	16.55
7.5	15947	0.48	0.92	−5.16	6.52	15.93	1.08	−5.11	6.54	15.99
7.5	18059	0.59	0.91	−6.57	6.25	14.51	1.07	−6.40	6.28	14.69
7.5	19931	0.78	0.97	−9.16	5.74	11.92	1.14	−8.72	5.83	12.36
7.5	22044	0.94	0.82	−11.06	5.42	10.02	0.95	−10.82	5.46	10.26
7.5	23774	1.02	0.69	−12.07	5.24	9.01	0.80	−11.62	5.33	9.45
8.0	12020	0.38	1.00	−5.21	6.59	16.87	1.00	−5.21	6.59	16.87
8.0	14083	0.42	1.00	−5.57	6.56	16.51	1.00	−5.57	6.56	16.51
8.0	16105	0.46	0.89	−6.08	6.48	16.00	1.04	−6.05	6.49	16.04
8.0	18082	0.52	0.83	−6.96	6.32	15.12	0.97	−6.86	6.34	15.23
8.0	20090	0.66	0.88	−8.71	5.98	13.37	1.03	−8.45	6.04	13.63
8.0	21014	0.66	0.89	−9.92	5.75	12.16	1.04	−9.56	5.82	12.52
8.0	21465	0.75	0.97	−10.38	5.67	11.70	1.14	−9.97	5.74	12.11
8.0	21987	0.78	1.10	−10.82	5.59	11.26	1.28	−10.38	5.67	11.70
8.0	22988	0.82	1.00	−11.39	5.49	10.68	1.17	−11.25	5.52	10.83
8.0	24144	0.82	0.78	−11.90	5.41	10.17	0.92	−11.69	5.45	10.38
8.0	25898	0.87	0.71	−12.61	5.30	9.46	0.83	−12.27	5.36	9.81
8.5	12139	0.37	1.00	−6.38	6.47	16.70	1.00	−6.38	6.47	16.70
8.5	14007	0.40	1.00	−6.64	6.47	16.44	1.00	−6.64	6.47	16.44
8.5	15961	0.43	1.00	−6.99	6.43	16.09	1.00	−6.99	6.43	16.09
8.5	18000	0.48	0.74	−7.60	6.33	15.47	0.87	−7.55	6.34	15.53
8.5	19955	0.55	0.77	−8.62	6.14	14.46	0.90	−8.47	6.17	14.60
8.5	22000	0.70	0.80	−10.56	5.77	12.52	0.94	−10.26	5.84	12.82
8.5	24143	0.82	1.16	−11.93	5.54	11.14	1.36	−11.65	5.59	11.43
8.5	25805	0.87	0.85	−12.50	5.45	10.57	0.99	−12.34	5.48	10.74
8.5	27934	0.94	0.70	−13.27	5.33	9.81	0.82	−12.97	5.38	10.10
9.0	12124	0.35	1.00	−7.69	6.28	16.39	1.00	−7.69	6.28	16.39
9.0	14117	0.38	1.00	−7.84	6.34	16.24	1.00	−7.84	6.34	16.24
9.0	16029	0.41	1.00	−8.09	6.33	15.99	1.00	−8.09	6.33	15.99
9.0	17998	0.45	0.77	−8.47	6.29	15.61	0.90	−8.44	6.30	15.64
9.0	19961	0.50	0.64	−9.18	6.17	14.90	0.75	−9.10	6.18	14.97
9.0	21978	0.59	0.75	−10.32	5.97	13.76	0.88	−10.13	6.01	13.94
9.0	24082	0.72	0.81	−12.00	5.66	12.08	0.95	−11.72	5.71	12.36
9.0	26109	0.79	1.13	−12.81	5.53	11.27	1.32	−12.58	5.57	11.49
9.0	28143	0.85	0.79	−13.41	5.43	10.67	0.92	−13.25	5.46	10.83
9.0	30184	0.89	0.74	−13.86	5.37	10.22	0.86	−13.63	5.41	10.45
9.0	31440	0.92	0.72	−14.18	5.32	9.90	0.84	−13.89	5.37	10.19

Table A8. Same as Tab. A7 but for MLT calibration of open bottom 3D DBA models with log H/He = −7.

$\log g$	$T_{\rm eff}$ (K)	3D $s_{\rm env}$ (10^9 erg g^{-1} K^{-1})	ML2/$\alpha_{\rm S}$	$\log(M_{\rm CVZ}/M_{\rm tot})_{\rm S}$	$(\log T_{\rm b})_{\rm S}$ (K)	$(\log P_{\rm b})_{\rm S}$ (dyn cm^{-2})	ML2/$\alpha_{\rm f}$	$\log(M_{\rm CVZ}/M_{\rm tot})_{\rm f}$	$(\log T_{\rm b})_{\rm f}$ (K)	$(\log P_{\rm b})_{\rm f}$ (dyn cm^{-2})
7.5	12098	0.40	1.00	−4.14	6.68	16.96	1.00	−4.14	6.68	16.96
7.5	13967	0.44	0.91	−4.56	6.63	16.53	1.06	−4.54	6.63	16.56
7.5	15936	0.48	0.91	−5.16	6.52	15.93	1.07	−5.11	6.54	15.99
7.5	18051	0.59	0.91	−6.57	6.25	14.51	1.06	−6.39	6.29	14.69
7.5	19865	0.79	0.91	−9.23	5.73	11.85	1.07	−8.76	5.82	12.32
7.5	21873	0.94	0.79	−11.06	5.41	10.02	0.92	−10.83	5.45	10.25
7.5	23789	1.02	0.69	−12.07	5.24	9.01	0.80	−11.62	5.33	9.45
8.0	12019	0.38	1.00	−5.21	6.59	16.87	1.00	−5.21	6.59	16.87
8.0	14083	0.42	1.00	−5.57	6.56	16.51	1.00	−5.57	6.56	16.51
8.0	16099	0.46	0.88	−6.08	6.48	16.00	1.03	−6.05	6.49	16.04
8.0	18074	0.52	0.82	−6.96	6.32	15.13	0.96	−6.86	6.34	15.23
8.0	20088	0.66	0.88	−8.71	5.98	13.37	1.03	−8.45	6.04	13.63
8.0	21996	0.82	1.10	−10.82	5.59	11.26	1.29	−10.38	5.67	11.70
8.0	24036	0.91	0.79	−11.87	5.42	10.21	0.93	−11.65	5.46	10.43
8.0	25956	0.97	0.71	−12.61	5.30	9.46	0.83	−12.27	5.36	9.81
8.5	12147	0.37	1.00	−6.38	6.47	16.69	1.00	−6.38	6.47	16.69
8.5	14004	0.40	1.00	−6.64	6.47	16.44	1.00	−6.64	6.47	16.44
8.5	15958	0.43	1.00	−6.99	6.43	16.09	1.00	−6.99	6.43	16.09
8.5	17998	0.48	0.74	−7.60	6.33	15.48	0.87	−7.55	6.34	15.53
8.5	19951	0.55	0.77	−8.62	6.14	14.46	0.90	−8.47	6.17	14.60
8.5	22002	0.70	0.80	−10.56	5.77	12.52	0.94	−10.26	5.84	12.82
8.5	24047	0.81	1.15	−11.90	5.54	11.17	1.35	−11.59	5.60	11.49
8.5	25943	0.87	0.83	−12.55	5.44	10.53	0.97	−12.38	5.47	10.69
8.5	27907	0.94	0.69	−13.27	5.33	9.81	0.81	−12.98	5.38	10.10
9.0	12120	0.35	1.00	−7.69	6.28	16.39	1.00	−7.69	6.28	16.39
9.0	14114	0.38	1.00	−7.84	6.34	16.24	1.00	−7.84	6.34	16.24
9.0	16026	0.41	1.00	−8.09	6.33	15.99	1.00	−8.09	6.33	15.99
9.0	17985	0.45	0.75	−8.47	6.29	15.61	0.88	−8.44	6.30	15.64
9.0	19957	0.50	0.64	−9.18	6.17	14.90	0.75	−9.10	6.18	14.97
9.0	21982	0.59	0.76	−10.32	5.97	13.76	0.89	−10.13	6.01	13.94
9.0	24093	0.72	0.81	−12.00	5.66	12.08	0.95	−11.72	5.71	12.36
9.0	26115	0.79	1.13	−12.81	5.53	11.27	1.33	−12.58	5.57	11.49
9.0	28141	0.85	0.79	−13.41	5.43	10.67	0.92	−13.25	5.46	10.83
9.0	30006	0.89	0.75	−13.80	5.38	10.27	0.87	−13.58	5.41	10.49
9.0	31472	0.92	0.72	−14.18	5.32	9.89	0.85	−13.89	5.37	10.19

Table A9. Same as Tab. A7 but for MLT calibration of open bottom 3D DBA models with $\log \mathrm{H/He} = -5$.

$\log g$	$T_{\rm eff}$ (K)	3D $s_{\rm env}$ (10^9 erg g^{-1} K^{-1})	ML2/$\alpha_{\rm S}$	$\log(M_{\rm CVZ}/M_{\rm tot})_{\rm S}$	$(\log T_{\rm b})_{\rm S}$ (K)	$(\log P_{\rm b})_{\rm S}$ (dyn cm^{-2})	ML2/$\alpha_{\rm f}$	$\log(M_{\rm CVZ}/M_{\rm tot})_{\rm f}$	$(\log T_{\rm b})_{\rm f}$ (K)	$(\log P_{\rm b})_{\rm f}$ (dyn cm^{-2})
7.5	12009	0.40	1.00	−4.13	6.69	16.98	1.00	−4.13	6.69	16.98
7.5	14013	0.44	0.85	−4.59	6.62	16.51	0.99	−4.56	6.63	16.54
7.5	15886	0.49	0.78	−5.22	6.51	15.88	0.91	−5.14	6.53	15.95
7.5	17920	0.59	0.82	−6.58	6.24	14.50	0.95	−6.40	6.28	14.68
7.5	19900	0.79	0.93	−9.24	5.73	11.84	1.09	−8.78	5.82	12.30
7.5	21946	0.94	0.80	−11.06	5.42	10.02	0.94	−10.83	5.46	10.25
7.5	23757	1.02	0.68	−12.07	5.24	9.01	0.80	−11.62	5.33	9.45
8.0	11978	0.38	1.00	−5.23	6.58	16.86	1.00	−5.23	6.58	16.86
8.0	14031	0.42	1.00	−5.56	6.56	16.52	1.00	−5.56	6.56	16.52
8.0	15974	0.46	0.74	−6.09	6.48	15.99	0.86	−6.05	6.49	16.04
8.0	17952	0.52	0.74	−6.97	6.31	15.11	0.86	−6.86	6.33	15.22
8.0	20012	0.66	0.84	−8.71	5.98	13.37	0.98	−8.45	6.04	13.63
8.0	21959	0.82	1.08	−10.82	5.59	11.26	1.27	−10.37	5.67	11.71
8.0	24014	0.91	0.79	−11.87	5.42	10.21	0.93	−11.65	5.46	10.43
8.0	25963	0.97	0.71	−12.61	5.30	9.46	0.83	−12.27	5.36	9.81
8.5	11996	0.36	1.00	−6.40	6.45	16.68	1.00	−6.40	6.45	16.68
8.5	14012	0.40	1.00	−6.66	6.46	16.42	1.00	−6.66	6.46	16.42
8.5	15957	0.43	1.00	−6.99	6.43	16.09	1.00	−6.99	6.43	16.09
8.5	17956	0.48	0.66	−7.65	6.32	15.43	0.77	−7.57	6.34	15.51
8.5	19924	0.56	0.74	−8.64	6.14	14.44	0.86	−8.51	6.16	14.57
8.5	21962	0.70	0.78	−10.56	5.78	12.52	0.92	−10.26	5.83	12.81
8.5	24004	0.81	1.13	−11.90	5.54	11.17	1.33	−11.58	5.60	11.50
8.5	25938	0.87	0.83	−12.55	5.44	10.53	0.97	−12.38	5.47	10.69
8.5	27946	0.94	0.70	−13.27	5.33	9.81	0.82	−12.97	5.38	10.10
9.0	12077	0.35	1.00	−7.68	6.28	16.40	1.00	−7.68	6.28	16.40
9.0	14059	0.38	1.00	−7.84	6.34	16.24	1.00	−7.84	6.34	16.24
9.0	15930	0.41	1.00	−8.07	6.33	16.01	1.00	−8.07	6.33	16.01
9.0	17885	0.45	0.65	−8.48	6.28	15.60	0.76	−8.45	6.29	15.63
9.0	19922	0.50	0.61	−9.20	6.16	14.87	0.71	−9.11	6.18	14.96
9.0	21942	0.59	0.74	−10.32	5.97	13.76	0.86	−10.13	6.01	13.94
9.0	24076	0.72	0.81	−12.01	5.66	12.07	0.94	−11.72	5.71	12.36
9.0	26099	0.79	1.13	−12.81	5.53	11.27	1.32	−12.58	5.57	11.50
9.0	28181	0.85	0.79	−13.41	5.43	10.66	0.93	−13.25	5.46	10.83
9.0	29952	0.89	0.74	−13.80	5.38	10.27	0.87	−13.58	5.41	10.50
9.0	31452	0.92	0.72	−14.18	5.32	9.89	0.84	−13.89	5.37	10.18

Table A10. Same as Tab. A7 but for MLT calibration of open bottom 3D DBA models with log H/He = −4.

$\log g$	$T_{\rm eff}$ (K)	3D $s_{\rm env}$ (10^9 erg g^{-1} K^{-1})	ML2/$\alpha_{\rm S}$	$\log(M_{\rm CVZ}/M_{\rm tot})_{\rm S}$	$(\log T_{\rm b})_{\rm S}$ (K)	$(\log P_{\rm b})_{\rm S}$ (dyn cm^{-2})	ML2/$\alpha_{\rm f}$	$\log(M_{\rm CVZ}/M_{\rm tot})_{\rm f}$	$(\log T_{\rm b})_{\rm f}$ (K)	$(\log P_{\rm b})_{\rm f}$ (dyn cm^{-2})
7.5	11983	0.40	1.00	−4.21	6.67	16.89	1.00	−4.21	6.67	16.89
7.5	13985	0.44	1.00	−4.61	6.62	16.48	1.00	−4.61	6.62	16.48
7.5	15973	0.49	0.85	−5.27	6.50	15.83	0.99	−5.21	6.51	15.88
7.5	17979	0.62	0.68	−7.01	6.16	14.08	0.79	−6.73	6.22	14.36
7.5	19932	0.82	0.86	−9.67	5.65	11.41	1.00	−9.11	5.75	11.97
7.5	22021	0.95	0.76	−11.16	5.40	9.92	0.89	−10.92	5.44	10.16
7.5	23465	1.01	0.68	−11.92	5.27	9.15	0.80	−11.53	5.35	9.55
8.0	12008	0.39	1.00	−5.30	6.57	16.78	1.00	−5.30	6.57	16.78
8.0	13999	0.42	1.00	−5.60	6.55	16.48	1.00	−5.60	6.55	16.48
8.0	15994	0.46	0.80	−6.11	6.47	15.97	0.93	−6.08	6.48	16.00
8.0	18052	0.54	0.63	−7.22	6.26	14.86	0.73	−7.08	6.29	15.00
8.0	19991	0.68	0.74	−8.98	5.92	13.10	0.86	−8.66	5.99	13.41
8.0	21981	0.83	1.05	−10.98	5.56	11.10	1.22	−10.50	5.65	11.57
8.0	23953	0.91	0.78	−11.88	5.42	10.20	0.91	−11.65	5.46	10.43
8.0	25961	0.97	0.71	−12.61	5.30	9.47	0.83	−12.27	5.36	9.81
8.5	12027	0.37	1.00	−6.45	6.45	16.63	1.00	−6.45	6.45	16.63
8.5	13981	0.40	1.00	−6.70	6.45	16.38	1.00	−6.70	6.45	16.38
8.5	15982	0.43	1.00	−7.04	6.42	16.04	1.00	−7.04	6.42	16.04
8.5	17951	0.49	0.57	−7.76	6.29	15.32	0.66	−7.67	6.31	15.41
8.5	19972	0.57	0.68	−8.81	6.11	14.27	0.79	−8.63	6.14	14.45
8.5	21956	0.72	0.73	−10.73	5.74	12.35	0.86	−10.39	5.81	12.68
8.5	23980	0.82	1.10	−11.95	5.53	11.13	1.28	−11.65	5.59	11.43
8.5	26006	0.88	0.82	−12.58	5.44	10.50	0.96	−12.41	5.46	10.67
8.5	27829	0.94	0.69	−13.26	5.33	9.82	0.80	−12.98	5.38	10.10
9.0	12055	0.35	1.00	−7.74	6.27	16.33	1.00	−7.74	6.27	16.33
9.0	14023	0.38	1.00	−7.88	6.33	16.20	1.00	−7.88	6.33	16.20
9.0	16020	0.41	1.00	−8.13	6.32	15.94	1.00	−8.13	6.32	15.94
9.0	17972	0.45	0.53	−8.57	6.27	15.50	0.62	−8.54	6.27	15.54
9.0	19968	0.51	0.56	−9.29	6.14	14.78	0.65	−9.20	6.16	14.87
9.0	21957	0.60	0.68	−10.45	5.94	13.62	0.79	−10.27	5.98	13.81
9.0	23971	0.72	0.77	−12.00	5.66	12.08	0.91	−11.72	5.71	12.36
9.0	26018	0.79	1.11	−12.80	5.53	11.27	1.29	−12.57	5.57	11.50
9.0	27982	0.84	0.80	−13.37	5.44	10.70	0.93	−13.23	5.46	10.85
9.0	29948	0.89	0.74	−13.81	5.38	10.27	0.87	−13.58	5.41	10.50
9.0	31360	0.92	0.71	−14.18	5.32	9.89	0.84	−13.89	5.37	10.18

Table A11. Same as Tab. A7 but for MLT calibration of open bottom 3D DBA models with $\log \mathrm{H/He} = -3$.

$\log g$	T_{eff} (K)	3D s_{env} (10^9 erg g^{-1} K^{-1})	ML2/α_{S}	$\log(M_{\mathrm{CVZ}}/M_{\mathrm{tot}})_{\mathrm{S}}$	$(\log T_{\mathrm{b}})_{\mathrm{S}}$ (K)	$(\log P_{\mathrm{b}})_{\mathrm{S}}$ (dyn cm^{-2})	ML2/α_{f}	$\log(M_{\mathrm{CVZ}}/M_{\mathrm{tot}})_{\mathrm{f}}$	$(\log T_{\mathrm{b}})_{\mathrm{f}}$ (K)	$(\log P_{\mathrm{b}})_{\mathrm{f}}$ (dyn cm^{-2})
7.5	11980	0.40	1.00	−4.56	6.59	16.54	1.00	−4.56	6.59	16.54
7.5	13855	0.44	1.00	−4.92	6.55	16.18	1.00	−4.92	6.55	16.18
7.5	15805	0.49	1.00	−5.51	6.45	15.58	1.00	−5.51	6.45	15.58
7.5	18026	0.59	1.18	−6.66	6.23	14.42	1.38	−6.50	6.26	14.59
7.5	20035	0.80	1.08	−9.39	5.70	11.69	1.27	−8.93	5.79	12.15
7.5	22043	0.94	0.81	−11.09	5.41	9.99	0.95	−10.85	5.45	10.23
7.5	23752	1.02	0.69	−12.05	5.25	9.02	0.81	−11.62	5.33	9.45
8.0	12007	0.38	1.00	−5.61	6.51	16.48	1.00	−5.61	6.51	16.48
8.0	13961	0.42	1.00	−5.92	6.48	16.16	1.00	−5.92	6.48	16.16
8.0	16040	0.46	1.00	−6.37	6.42	15.72	1.00	−6.37	6.42	15.72
8.0	17985	0.52	1.00	−7.13	6.28	14.95	1.00	−7.13	6.28	14.95
8.0	20088	0.66	1.02	−8.79	5.96	13.29	1.19	−8.53	6.02	13.55
8.0	22047	0.83	1.17	−10.89	5.57	11.18	1.37	−10.44	5.66	11.63
8.0	24002	0.91	0.79	−11.88	5.42	10.20	0.93	−11.66	5.45	10.42
8.0	25904	0.97	0.71	−12.61	5.30	9.47	0.83	−12.27	5.36	9.81
8.5	12027	0.37	1.00	−6.74	6.41	16.34	1.00	−6.74	6.41	16.34
8.5	13985	0.40	1.00	−6.96	6.40	16.11	1.00	−6.96	6.40	16.11
8.5	15988	0.43	1.00	−7.28	6.37	15.80	1.00	−7.28	6.37	15.80
8.5	18029	0.48	1.00	−7.80	6.29	15.28	1.00	−7.80	6.29	15.28
8.5	20043	0.56	1.02	−8.71	6.12	14.37	1.19	−8.57	6.15	14.51
8.5	22050	0.71	0.88	−10.63	5.77	12.45	1.03	−10.36	5.81	12.72
8.5	24011	0.81	1.18	−11.90	5.54	11.18	1.38	−11.61	5.59	11.47
8.5	25884	0.87	0.83	−12.56	5.44	10.52	0.97	−12.38	5.47	10.69
8.5	27602	0.94	0.67	−13.26	5.33	9.81	0.79	−12.97	5.38	10.10
9.0	11994	0.35	1.00	−8.06	6.22	16.02	1.00	−8.06	6.22	16.02
9.0	13967	0.38	1.00	−8.14	6.27	15.94	1.00	−8.14	6.27	15.94
9.0	15970	0.41	1.00	−8.32	6.28	15.75	1.00	−8.32	6.28	15.75
9.0	18038	0.45	1.00	−8.65	6.25	15.43	1.00	−8.65	6.25	15.43
9.0	20045	0.50	0.98	−9.24	6.15	14.83	1.15	−9.18	6.17	14.90
9.0	22057	0.60	0.90	−10.40	5.95	13.68	1.05	−10.23	5.99	13.84
9.0	24026	0.72	0.86	−11.97	5.67	12.11	1.01	−11.70	5.72	12.38
9.0	25997	0.79	1.15	−12.79	5.53	11.29	1.35	−12.57	5.57	11.51
9.0	28015	0.85	0.78	−13.42	5.43	10.65	0.91	−13.25	5.46	10.82
9.0	29929	0.89	0.73	−13.85	5.37	10.23	0.85	−13.62	5.41	10.46
9.0	31340	0.92	0.70	−14.23	5.31	9.84	0.82	−13.93	5.36	10.15

Table A12. Same as Tab. A7 but for MLT calibration of open bottom 3D DBA models with log H/He = −2.

$\log g$	$T_{\rm eff}$ (K)	3D $s_{\rm env}$ (10^9 erg g^{-1} K^{-1})	ML2/$\alpha_{\rm S}$	$\log(M_{\rm CVZ}/M_{\rm tot})_{\rm S}$	$(\log T_{\rm b})_{\rm S}$ (K)	$(\log P_{\rm b})_{\rm S}$ (dyn cm^{-2})	ML2/$\alpha_{\rm f}$	$\log(M_{\rm CVZ}/M_{\rm tot})_{\rm f}$	$(\log T_{\rm b})_{\rm f}$ (K)	$(\log P_{\rm b})_{\rm f}$ (dyn cm^{-2})
7.5	11977	0.45	1.00	−5.24	6.44	15.85	1.00	−5.24	6.44	15.85
7.5	13995	0.49	1.00	−5.84	6.35	15.24	1.00	−5.84	6.35	15.24
7.5	16063	0.56	1.00	−6.97	6.15	14.11	1.00	−6.97	6.15	14.11
7.5	17963	0.68	1.00	−8.78	5.80	12.30	1.00	−8.78	5.80	12.30
7.5	20042	0.88	1.11	−10.38	5.52	10.70	1.30	−10.23	5.55	10.85
7.5	21944	0.98	0.68	−11.49	5.34	9.59	0.80	−11.19	5.39	9.89
7.5	22925	1.02	0.65	−12.00	5.25	9.08	0.76	−11.60	5.33	9.48
8.0	12044	0.43	1.00	−6.26	6.37	15.82	1.00	−6.26	6.37	15.82
8.0	13953	0.46	1.00	−6.63	6.33	15.45	1.00	−6.63	6.33	15.45
8.0	15983	0.50	1.00	−7.28	6.22	14.80	1.00	−7.28	6.22	14.80
8.0	17961	0.58	1.00	−8.44	6.01	13.64	1.00	−8.44	6.01	13.64
8.0	19903	0.74	1.11	−9.87	5.75	12.21	1.29	−9.50	5.82	12.58
8.0	22026	0.88	0.81	−11.55	5.46	10.53	0.94	−11.40	5.48	10.67
8.0	24006	0.94	0.69	−12.21	5.36	9.86	0.81	−11.96	5.40	10.12
8.0	25333	0.98	0.68	−12.64	5.29	9.43	0.80	−12.30	5.35	9.78
8.5	12013	0.41	1.00	−7.34	6.28	15.74	1.00	−7.34	6.28	15.74
8.5	14013	0.44	1.00	−7.57	6.28	15.51	1.00	−7.57	6.28	15.51
8.5	15994	0.47	1.00	−8.00	6.22	15.08	1.00	−8.00	6.22	15.08
8.5	17996	0.52	1.00	−8.70	6.10	14.37	1.00	−8.70	6.10	14.37
8.5	19962	0.63	1.00	−9.84	5.90	13.24	1.00	−9.84	5.90	13.24
8.5	22044	0.80	0.93	−11.73	5.56	11.35	1.09	−11.28	5.64	11.80
8.5	24025	0.86	0.81	−12.38	5.46	10.70	0.95	−12.23	5.48	10.84
8.5	25969	0.90	0.73	−12.83	5.39	10.25	0.86	−12.63	5.43	10.45
8.5	27179	0.94	0.66	−13.30	5.32	9.78	0.77	−13.01	5.37	10.07
9.0	12025	0.39	1.00	−8.53	6.15	15.54	1.00	−8.53	6.15	15.54
9.0	13986	0.42	1.00	−8.63	6.19	15.44	1.00	−8.63	6.19	15.44
9.0	16001	0.45	1.00	−8.89	6.18	15.19	1.00	−8.89	6.18	15.19
9.0	17981	0.48	1.00	−9.35	6.11	14.73	1.00	−9.35	6.11	14.73
9.0	20038	0.55	1.00	−10.07	6.00	14.00	1.00	−10.07	6.00	14.00
9.0	21923	0.68	0.79	−11.51	5.73	12.56	0.93	−11.23	5.79	12.85
9.0	24031	0.78	0.94	−12.65	5.54	11.43	1.10	−12.31	5.60	11.77
9.0	26031	0.83	0.84	−13.18	5.46	10.90	0.98	−13.05	5.48	11.02
9.0	27980	0.87	0.71	−13.61	5.40	10.47	0.83	−13.43	5.43	10.65
9.0	29843	0.91	0.69	−14.00	5.34	10.07	0.81	−13.75	5.38	10.33
9.0	31011	0.93	0.69	−14.28	5.30	9.79	0.80	−14.00	5.35	10.08

Table A13. MLT calibration for closed bottom 3D DB models, where ⟨3D⟩ $T_{\rm b,\,S}$ is the ⟨3D⟩ temperature at the bottom of the Schwarzschild boundary, ⟨3D⟩ $P_{\rm b,\,S}$ is the ⟨3D⟩ pressure at the bottom of the Schwarzschild boundary, ML2/$\alpha_{\rm S}$ is the calibrated ML2/α value for the Schwarzschild boundary and $\log(M_{\rm CVZ}/M_{\rm tot})_{\rm S}$ is the $\log(M_{\rm CVZ}/M_{\rm tot})$ for the Schwarzschild boundary. The same parameters are also given for the flux boundary and are denoted with a subscript 'f'.

$\log g$	$T_{\rm eff}$	⟨3D⟩ $T_{\rm b,\,S}$	⟨3D⟩ $P_{\rm b,\,S}$	ML2/$\alpha_{\rm S}$	$\log(M_{\rm CVZ}/M_{\rm tot})_{\rm S}$	⟨3D⟩ $T_{\rm b,\,f}$	⟨3D⟩ $P_{\rm b,\,f}$	ML2/$\alpha_{\rm f}$	$\log(M_{\rm CVZ}/M_{\rm tot})_{\rm f}$
7.5	26497	4.98	7.85	0.76	−13.20	5.10	8.28	0.85	−12.76
7.5	27993	4.90	7.45	0.69	−13.63	4.95	7.66	0.85	−13.41
7.5	29991	4.87	7.24	0.42	−13.84	4.86	7.19	0.65	−13.82
7.5	32001	4.87	7.15	0.65	−13.91	4.85	7.08	0.65	−13.91
8.0	28107	4.99	8.21	0.65	−13.94	5.14	8.74	0.75	−13.36
8.0	29997	4.94	7.86	0.72	−14.24	5.03	8.24	0.85	−13.84
8.0	31999	4.91	7.62	0.73	−14.47	4.94	7.76	0.89	−14.31
8.0	33999	4.89	7.43	0.65	−14.63	4.87	7.35	0.65	−14.63
8.5	30567	5.03	8.58	0.63	−14.59	5.20	9.14	0.74	−13.96
8.5	32208	5.00	8.32	0.71	−14.80	5.12	8.77	0.81	−14.33
8.5	34020	4.95	8.00	0.75	−15.09	5.02	8.27	0.87	−14.80
9.0	34105	5.05	8.78	0.64	−15.38	5.21	9.28	0.75	−14.81

Table A14. Same as Tab. A13 but for MLT calibration of closed bottom 3D DBA models with log H/He = −7.

$\log g$	$T_{\rm eff}$	$\langle 3D \rangle$ $T_{\rm b,\ S}$	$\langle 3D \rangle$ $P_{\rm b,\ S}$	ML2/$\alpha_{\rm S}$	$\log{(M_{\rm CVZ}/M_{\rm tot})_{\rm S}}$	$\langle 3D \rangle$ $T_{\rm b,\ f}$	$\langle 3D \rangle$ $P_{\rm b,\ f}$	ML2/$\alpha_{\rm f}$	$\log{(M_{\rm CVZ}/M_{\rm tot})_{\rm f}}$
7.5	26501	4.98	7.84	0.75	−13.21	5.11	8.29	0.85	−12.75
7.5	27993	4.90	7.46	0.70	−13.63	4.95	7.66	0.85	−13.40
7.5	29993	4.87	7.25	0.57	−13.83	4.87	7.21	0.65	−13.82
7.5	32002	4.87	7.16	0.65	−13.91	4.85	7.06	0.65	−13.91
8.0	28037	4.98	8.18	0.64	−13.97	5.13	8.72	0.75	−13.38
8.0	29963	5.00	8.04	0.80	−14.01	5.12	8.49	0.90	−13.55
8.0	32000	4.91	7.60	0.71	−14.48	4.94	7.73	0.86	−14.35
8.0	33999	4.89	7.43	0.65	−14.63	4.87	7.35	0.65	−14.63
8.5	30514	5.03	8.59	0.63	−14.58	5.21	9.15	0.74	−13.94
8.5	32012	4.99	8.33	0.70	−14.80	5.14	8.83	0.80	−14.26
8.5	33949	4.95	8.00	0.74	−15.09	5.02	8.28	0.87	−14.79
9.0	34021	5.06	8.82	0.65	−15.33	5.21	9.29	0.75	−14.79

Table A15. Same as Tab. A13 but for MLT calibration of closed bottom 3D DBA models with log H/He = −5.

$\log g$	$T_{\rm eff}$	$\langle 3D \rangle$ $T_{\rm b,\ S}$	$\langle 3D \rangle$ $P_{\rm b,\ S}$	ML2/$\alpha_{\rm S}$	$\log{(M_{\rm CVZ}/M_{\rm tot})_{\rm S}}$	$\langle 3D \rangle$ $T_{\rm b,\ f}$	$\langle 3D \rangle$ $P_{\rm b,\ f}$	ML2/$\alpha_{\rm f}$	$\log{(M_{\rm CVZ}/M_{\rm tot})_{\rm f}}$
7.5	26522	4.97	7.83	0.75	−13.23	5.10	8.27	0.85	−12.77
7.5	27998	4.90	7.46	0.70	−13.63	4.95	7.66	0.85	−13.41
7.5	29992	4.87	7.25	0.49	−13.84	4.86	7.19	0.65	−13.82
7.5	32002	4.87	7.16	0.65	−13.91	4.85	7.08	0.65	−13.91
8.0	28086	4.98	8.19	0.65	−13.95	5.13	8.73	0.75	−13.38
8.0	29989	4.94	7.87	0.72	−14.24	5.03	8.24	0.85	−13.84
8.0	32002	4.91	7.61	0.71	−14.48	4.94	7.75	0.88	−14.32
8.0	34000	4.89	7.43	0.65	−14.63	4.87	7.35	0.65	−14.63
8.5	30517	5.02	8.59	0.63	−14.58	5.21	9.16	0.74	−13.93
8.5	32015	5.00	8.36	0.71	−14.76	5.14	8.83	0.80	−14.27
8.5	33947	4.95	8.00	0.74	−15.09	5.02	8.29	0.87	−14.78
9.0	33986	5.06	8.82	0.65	−15.33	5.21	9.30	0.75	−14.79

Table A16. Same as Tab. A13 but for MLT calibration of closed bottom 3D DBA models with log H/He = −4.

$\log g$	$T_{\rm eff}$ (K)	$\langle 3D \rangle$ $T_{\rm b,\ S}$ (K)	$\langle 3D \rangle$ $P_{\rm b,\ S}$ (dyn cm^{-2})	ML2/$\alpha_{\rm S}$	$\log{(M_{\rm CVZ}/M_{\rm tot})_{\rm S}}$	$\langle 3D \rangle$ $T_{\rm b,\ f}$ (K)	$\langle 3D \rangle$ $P_{\rm b,\ f}$ (dyn cm^{-2})	ML2/$\alpha_{\rm f}$	$\log{(M_{\rm CVZ}/M_{\rm tot})_{\rm f}}$
7.5	26632	4.97	7.81	0.76	−13.24	5.09	8.23	0.86	−12.81
7.5	28004	4.90	7.45	0.69	−13.64	4.94	7.64	0.84	−13.43
7.5	29993	4.87	7.25	0.51	−13.84	4.86	7.19	0.65	−13.82
7.5	32002	4.87	7.15	0.65	−13.91	4.85	7.07	0.65	−13.91
8.0	28092	4.98	8.17	0.64	−13.97	5.12	8.68	0.74	−13.42
8.0	29994	4.94	7.87	0.72	−14.23	5.04	8.25	0.85	−13.82
8.0	32003	4.91	7.60	0.71	−14.48	4.94	7.73	0.86	−14.35
8.0	34000	4.89	7.43	0.65	−14.63	4.87	7.35	0.65	−14.63
8.5	30490	5.03	8.61	0.63	−14.56	5.20	9.15	0.73	−13.95
8.5	32008	5.00	8.35	0.71	−14.77	5.13	8.81	0.80	−14.29
8.5	33963	4.95	8.00	0.75	−15.09	5.01	8.27	0.87	−14.80
9.0	33988	5.06	8.83	0.65	−15.33	5.21	9.30	0.75	−14.79

Table A17. Same as Tab. A13 but for MLT calibration of closed bottom 3D DBA models with log H/He = −3.

$\log g$	$T_{\rm eff}$ (K)	$\langle 3D \rangle\ T_{\rm b,\ S}$ (K)	$\langle 3D \rangle\ P_{\rm b,\ S}$ (dyn cm^{-2})	ML2/$\alpha_{\rm S}$	$\log{(M_{\rm CVZ}/M_{\rm tot})_{\rm S}}$	$\langle 3D \rangle\ T_{\rm b,\ f}$ (K)	$\langle 3D \rangle\ P_{\rm b,\ f}$ (dyn cm^{-2})	ML2/$\alpha_{\rm f}$	$\log{(M_{\rm CVZ}/M_{\rm tot})_{\rm f}}$
7.5	26670	4.95	7.74	0.74	−13.34	5.06	8.15	0.85	−12.91
7.5	28000	4.90	7.44	0.69	−13.65	4.94	7.61	0.83	−13.45
7.5	29999	4.87	7.24	0.54	−13.84	4.85	7.15	0.65	−13.82
7.5	32000	4.87	7.15	0.65	−13.92	4.84	7.05	0.65	−13.92
8.0	28118	4.98	8.14	0.64	−13.99	5.11	8.64	0.74	−13.45
8.0	30001	4.94	7.83	0.71	−14.27	5.02	8.18	0.84	−13.90
8.0	31999	4.90	7.58	0.67	−14.51	4.93	7.68	0.82	−14.40
8.0	33980	4.89	7.43	0.65	−14.63	4.87	7.36	0.65	−14.63
8.5	30364	5.03	8.59	0.62	−14.58	5.20	9.14	0.72	−13.96
8.5	31965	4.99	8.30	0.69	−14.81	5.12	8.77	0.79	−14.31
8.5	34038	4.95	7.99	0.75	−15.10	5.01	8.26	0.88	−14.81
9.0	33917	5.06	8.84	0.65	−15.31	5.21	9.31	0.75	−14.77

Table A18. Same as Tab. A13 but for MLT calibration of closed bottom 3D DBA models with log H/He = −2.

$\log g$	$T_{\rm eff}$ (K)	$\langle 3D \rangle\ T_{\rm b,\ S}$ (K)	$\langle 3D \rangle\ P_{\rm b,\ S}$ (dyn cm^{-2})	ML2/$\alpha_{\rm S}$	$\log{(M_{\rm CVZ}/M_{\rm tot})_{\rm S}}$	$\langle 3D \rangle\ T_{\rm b,\ f}$ (K)	$\langle 3D \rangle\ P_{\rm b,\ f}$ (dyn cm^{-2})	ML2/$\alpha_{\rm f}$	$\log{(M_{\rm CVZ}/M_{\rm tot})_{\rm f}}$
7.5	26471	4.93	7.67	0.71	−13.43	5.02	8.04	0.84	−13.04
7.5	27996	4.89	7.38	0.67	−13.70	4.91	7.50	0.80	−13.57
7.5	29982	4.87	7.22	0.65	−13.84	4.85	7.13	0.65	−13.84
7.5	32009	4.86	7.12	0.65	−13.93	4.84	7.04	0.65	−13.93
8.0	27968	4.96	8.07	0.65	−14.05	5.09	8.54	0.75	−13.56
8.0	30013	4.93	7.77	0.71	−14.32	4.99	8.06	0.86	−14.01
8.0	31998	4.90	7.53	0.61	−14.55	4.91	7.58	0.74	−14.50
8.0	33989	4.88	7.41	0.65	−14.65	4.86	7.33	0.65	−14.65
8.5	30535	5.01	8.45	0.64	−14.69	5.17	8.99	0.75	−14.10
8.5	31852	4.98	8.25	0.70	−14.86	5.10	8.70	0.81	−14.39
8.5	33930	4.94	7.95	0.75	−15.14	5.00	8.20	0.89	−14.87
9.0	33770	5.05	8.78	0.66	−15.36	5.20	9.27	0.76	−14.81